Hardin, R.A., and Beckermann, C., "Effect of Porosity on Mechanical Properties of 8630 Cast Steel," in Proceedings of the 58th SFSA Technical and Operating Conference, Paper No. 4.4, Steel Founders' Society of America, Chicago, IL, 2004.

# EFFECT OF POROSITY ON MECHANICAL PROPERTIES OF 8630 CAST STEEL

R.A. Hardin[1] and C. Beckermann[2]

[1]Research Engineer, Mechanical and Industrial Engineering Dept. The University of Iowa
[2]Professor, Mechanical and Industrial Engineering Dept. The University of Iowa

## Abstract

Porosity is measured from radiographs of 8630 steel fatigue test specimens taken prior to fatigue testing. The measurement procedure uses an in situ calibration method based on the specimens themselves to determine the relationship between the indications on the radiographs and thickness of steel. Measured porosity dimensions from the radiographs are found to agree well with measurements made on a cut and polished specimen surface. By summing the specimen porosity measurements over a specimen cross-section, a cross-sectional porosity versus specimen length distribution is determined. The maximum cross-sectional porosity found in the specimens in this study range from about 15% to 65% based on the radiographic analysis. Cross-sectional porosity distributions determined from two radiographic views of the specimens show excellent agreement and demonstrate the method's repeatability. The maximum cross-sectional porosity in the radiographs is found to correlate well with the fatigue test specimens' measured elastic modulus. Converting the elastic modulus measurements to an apparent porosity in the specimen, a close to one-to-one correspondence is found between this apparent porosity and the maximum cross-sectional porosity in the specimens. The average specimen porosity determined from the radiographs does not correlate with the measured elastic modulus. Fatigue test results are compared with the radiographic analysis by determining the fatigue notch factors of the test specimens based on their measured fatigue lives, test conditions, measured elastic modulus and other properties. Comparison between the notch factor and porosity from the radiographs shows a good correlation, but this result is specific to the fatigue test specimen geometry used. In preliminary work to compare measured the fatigue notch factors determined from the test results and handbook values, an equivalent porosity to specimen diameter ratio is calculated and compared with textbook stress concentration factors. This comparison shows that the fatigue test results for specimens with macroporosity fall between the effect of a transverse hole and a spherical hole in a round bar. Based on this preliminary finding, a more in-depth investigation of the effect of porosity dimensions on fatigue life in currently underway.

## Introduction

There is currently no standard or well-accepted engineering methodology that provides design engineers guidance for determining the effect of porosity on the mechanical performance of steel castings. Likewise there are no guidelines relating non-destructive testing or non-destructive examination (NDT or NDE) methods such as radiography to the performance of cast steel components. Unless design engineers have ample test data for the part, a track record of experience for a given part, or leading edge computational models and property data, designers are probably requesting that castings pass specified NDT standards without knowing exactly how this translates to part performance in service.

Designers of castings may specify that critical interior regions of castings be radiographically or ultrasonically sound. At critical surface regions of the casting, it may be specified that only castings free of surface or near surface defects found through liquid penetrant, magnetic particle or eddy current testing pass inspection. Experienced designers may then specify that less critical areas of the part can meet a lower degree of soundness requirement, for example ASTM Level 3 or better. Integration of casting soundness information into the design of castings is still ad-hoc and based on case-by-case experience, and has not advanced much beyond this point despite great interest in the topic for many years. Ideally, using the benefit of design "experience" and performance data that is typically available only for long-run, mass-produced components in a general way for all steel castings will lead to more confidence in casting designs, a more rational use of testing specifications, better performing castings and more castings being used. Developing engineering guidelines that integrate knowledge about the effects of porosity into casting design, production and NDT is the ultimate goal of the present work.

Porosity is not the only inhomogeneity that casting designers and foundry personnel are concerned about. Inclusions, notches and metal fins may also arise during casting, and in the cleaning room welding and grinding may introduce features that affect fatigue resistance.[1] Most casting simulations programs currently predict the average amount of porosity present in a computational volume of material. The nature of these predictions has been until recently fairly approximate; calculated through the use of algorithms based feeding paths/zones and critical solid-fractions that cut off feeding paths and generate porosity. Average volumetric porosity, even if accurate, would not give all the information on pore size and shape necessary to apply fatigue models. Recent developments in casting process simulation[2] allow for prediction of porosity due to gas-related and shrinkage-driven mechanisms, and physically realistic pore nucleation and growth modeling result in prediction of characteristic pore size and shape, in addition to more accurate volumetric porosity prediction. Such information, now available from casting simulation, can be integrated into casting mechanical performance modeling. Provided the necessary strength/fatigue models and property data exist for incorporation of the casting simulation results, engineers will soon have new tools to design high performance steel castings with confidence.

In a paper given at last year's SFSA T&O Conference[3], a more thorough review of the literature in the area of component life prediction in the presence of porosity was given than will

be given here. The most commonly used methods to predict the fatigue life of castings with porosity are:

1) Modeling pores as "equivalent" notches or cracks and determining the local strain arising from the effect of the notch and applying strain-life concepts to predict fatigue life.

2) Modeling the porosity as pre-existing cracks within the component, and using linear elastic fracture mechanics (LEFM) to predict crack propagation.

Method 1) is sometimes termed "crack initiation" life prediction. Using this prediction method alone assumes that crack initiation consumes the majority of the fatigue life. Predictions of component life using Method 2) assume crack propagation consumes most of the life. Combining both methods of prediction produces the so-called "total life" of the component, "initiation life" plus "propagation life".

Method 1) is the older of the two methods.[4-6] In an effort that preceded the current work by about 40 years, it was used to try to establish engineering methods relating weld performance to porosity detected in welds using radiographic standards.[7] An excellent example in the more recent literature applying and comparing both methods to cast steel is given by Heuler et al.[8] Recently there has been increasing interest in research on prediction of performance of castings with porosity. Most notably, Horstemeyer, McDowell, and co-workers[9-12] have been developing and applying leading edge fracture mechanics micro-plasticity models of fatigue and failure to incorporate effects of inclusions, microporosity, macroporosity and microstructure to cast aluminum alloy components. The work of Horstemeyer et al.[9-12] represents the state-of-the art in fracture mechanics modeling of the effects porosity on casting mechanical performance. How directly applicable this work is to steel castings remains to be seen. Additional research into properties, model parameters and validation studies using steel must be undertaken before it could be applied to steel with confidence.

In this paper, a procedure is presented for quantitatively analyzing the porosity of 8630 steel test specimens based on radiographs taken of the specimens before testing. Then the specimens' porosity is compared to material property data measured during fatigue testing of the specimens. Observations and comparisons are also made between the radiography of the specimens, their measured fatigue life and comparison with strain-life calculations of the specimens.

## Experimental and Analytical Procedure

### Fatigue Specimens and Fatigue Testing

In this investigation AISI 8630 quenched and tempered cast steel is studied. The details of production of the cast steel specimens and testing is given elsewhere.[3,13] Only a very brief description will be given here. Specimens having distributed microporosity were produced by casting the geometry shown in Figure 1(a), and those with macroporosity were cast using the

geometry shown in Figure 1(b). Three levels of porosity severity were designed into the castings as described in Figure 1. For the purposes of this paper, macroporosity is defined as porosity large enough to be detected by radiographic inspection. The castings were machined into round test specimens according to ASTM E606[14] standards, with the final polished dimensions provided in Figure 2.

All cast blanks received the following heat treatment; normalized at 900° C, austenized at 885° C, water quenched, and finally tempered for one and one half hours at 510° C. This resulted in a tempered martensitic structure with Rockwell C hardness of 34. The heat treatment was so chosen to be the same process used in an earlier 1982 SFSA report,[15] in order to create specimens with similar material properties to this baseline data. The specimens from the 1982 SFSA report were machined from large cast trapezoidal-shaped keel blocks, and data from the 1982 study will be referred to as the "sound" specimen data throughout the remainder of this paper.

Fatigue testing to determine the cyclic and fatigue properties of the specimens with microporosity began using the strain controlled low cycle fatigue (LCF) test procedure outlined in E 606.[14] The testing was changed to load control for the purposes of increasing testing speed after it was determined that the behavior of the specimens was predominately elastic. This made it possible to accurately determine strain amplitudes while using the faster testing capability of load control. All macroporosity testing was performed using load control at 10-20 Hz. An extensometer was used on these tests to produce readings for the elastic modulus, E. This data was used to determine a relationship between the apparent elastic modulus and the porosity measured from radiography. The specimens with macroporosity were run at four stress levels. The first stress level chosen was 126 MPa, the run-out stress amplitude for the specimens with microporosity. The second stress level of 66 MPa was chosen by converting the ε-N curve of the microporosity specimens to a stress-life curve, S-N, and then shifting this curve down to the lives of the specimens with macroporosity previously tested. This adjusted S-N curve was then used to estimate stress amplitude and lives of the specimens with macroporosity. The goal was to obtain a life on the order of $10^6$ cycles without run-outs occurring. The two remaining stress levels were chosen to fill in gaps within the macroporosity specimen data. All fatigue tests were performed until fracture of the specimen occurred, or a run-out life at $5x10^6$ cycles was achieved.

## Procedures for Test Specimen Radiography

The project was fortunate to have Alloy Weld Inspection Co. agree to perform digital and film radiography of the fatigue test specimens using a Fuji digital x-ray system. Unfortunately, due to problems with the digital radiograph storage, the digital radiographs could never be retrieved. The film radiographs produced by the digital system have 8-bit gray level images, having 256 gray levels. Because of the problems retrieving the digital radiographs, the film radiographs were "re-digitized" at the University of Iowa using a flatbed scanner at 1200 dots (or pixels) per inch (dpi). A customized backlighting of the radiograph, with an intense and diffuse light source, was necessary to achieve good scanning results. Using this technique, digital images of radiographs of good quality were stored for later analysis. Because of the 8-bits of gray level resolution in the original film radiographs, the total possible discrete levels of steel thickness in each radiograph would be limited to 256.

Example results of the radiographs for the range of porosities analyzed in this study are shown in Figure 3 for specimens with microporosity, and "least", "middle", and "most" macroporosity specimens. These four "classes" of specimens are defined by their geometry, as discussed above. Additionally, since each mold box rigging held two specimens each of microporosity, "middle", and "most" specimen types, the position of each specimen in the mold box was accounted for using letters to signify the position of the casting in the mold box. The letters used to signify these "families" of specimens were: "A" and "B" for specimens with microporosity, "C" for specimens with "least" macroporosity, "D" and "E" for specimens with "most" macroporosity, and "G" and "H" for specimens with "middle" macroporosity.

Each family of specimens was laid out together by hand above the radiographic film in left-to-right increasing numerical order. Lead characters were used to indicate the specimen family and the specimens' numbers. Each specimen had an "X" etched into the specimen end at a reference point about the specimen's periphery. Two orthogonal views of the specimens were shot for each specimen family one with the "X" positioned toward the x-ray source, and the second view was shot with the specimen rotated by hand approximately 90 degrees from the first view as shown in Figure 4. In Figures 5 and 6, the two resulting digitized radiographs for specimen family "C" are shown for example. The measured modulus and fatigue notch factor for each specimen are also given in the figure for future reference.

## Procedures for Radiographic Analysis: General Overview

In order to perform a quantitative analysis of the radiographs, a method to determine the relationship between the indications on the specimen radiographs and porosity was developed. The absorption of x-rays depends upon the energy of the x-rays and the type of material and thickness (or effective density) of material through which it passes. Also, the gray level intensity on the radiographs, caused by the x-ray energy that is not absorbed by the material, can be manipulated further by exposure parameters and film sensitivity. In the current study, no noticeable variation in the x-ray energy across any given radiograph could be determined (i.e. due to the spreading of the cone of the beam from the x-ray source). The procedure for confirming this will be described later. Also, for a given radiograph, the exposure settings and sensitivity should be relatively constant for the entire image. This may sound like a trivial concern, but, because of the re-digitization process, there may be some small variability here due to non-uniform backlighting. This leaves the primary variable driving the x-ray absorption in the specimens as the thickness, or effective density, of material through which the x-ray passes. Even though indications on the radiograph can also be thought of as "point density" indications/measurements; in this work "thickness" of the material is used a matter of convention in presenting the procedures and analysis. "Thickness" of material is the physical quantity on which the calibration of the radiographs is based. Also, "thickness" has the added advantage that it can be used to assign dimensions to the porosity for the purpose of defining notch sizes.

To complete the analysis of porosity from the radiographs, one needs to perform the following procedures:

1. Determine a relationship (calibration curve) of the radiograph gray level versus material (steel) thickness for the image by using radiographically sound material of known thickness as reference data.

2. Determine at a given point in the specimen what the material thickness is from the radiograph using the relationship in step 1.

3. Determine what the material thickness of the specimen should be at the point mentioned above in Step 2, if the material were completely sound through use of known specimen geometry.

4. By taking the difference between what the thickness should be if sound (Step 3) and what the thickness is (Step 2), we can determine how much material is missing at that point in the specimen. This will be the porosity.

The 0.18 inch thick penetrameters that were placed in each radiograph were of little use for quantitative analysis of the radiographs. They provide only one gage of thickness from which to determine the relationship between image gray level intensity and material thickness. Also, the penetrameter was made of stainless steel, and even though the x-ray absorption characteristic of steel and stainless steel are very similar, it was decided not to use the penetrameters to determine the thickness versus gray level on radiograph relationship. Further more, because of the nature of the re-digitization process, it was not surprising to find that each radiograph had slightly different exposure conditions. Therefore, a method for completing necessary steps outlined above was devised where the specimens on the radiograph themselves would be used for calibration, with reference thickness data taken from each radiograph. This way variability from radiograph to radiograph would not be a concern.

Since the cross-section of material through which the x-rays pass is circular (see Figure 7 a) and b)), the thickness of material would correspond to the path of a chord of a circle. The resulting gray level distribution on the radiograph for an entire radiographically sound test specimen is shown in Figure 3 a), and a demonstrative plot of the gray level distribution across the specimen test section relative to the specimen center is shown in Figure 7 c). In Figure 7c) the gray level plot is given at a discrete position along the specimen length. The plot has the highest gray level value (darkest) where there is no material between the x-ray source and the film. From the specimen edge to its center, the gray level decreases (lightens) to the lowest value at the specimen center, and then increases again to the opposite edge. For a sound specimen, the distribution about the center of the specimen is symmetric, and curve fitting the gray level/thickness distribution to any convenient symmetric distribution (Gaussian for instance) could serve as a way to accurately determine the center of the gray level distribution, and cross-section of the specimen, on the radiographs. Once the center of the test specimen is known on the radiograph, from specimen geometry and position the thickness of the steel in the sound sections can be determined. All “sound” thickness versus gray scale data can then be compiled, and an in-situ calibration can be performed for a section of sound material, for a given specimen. The calibration curve establishes Step 1, and serves as the basis for Step 2, and determination of the specimen center allows for the completion of Step 3, as outlined above.

In Figure 7 d) a schematic drawing for the case of a section of material with porosity is shown. Note that the combined thickness of "unsound" material $t_{unsound}$ in the presence of porosity is represented as having three discrete segments. Unfortunately, the radiograph will give only the "total" thickness of unsound material, or a density measurement through the specimen. It will not tell you if the material has one discrete hole or a finer, but more sizable, network of macroporosity; multiple views and ultimately x-ray tomography would be required for this type of information. The resulting gray scale versus position plot for this example cross-section is shown in Figure 7 e). Where the porosity occurs, there is a large increase in the gray scale level corresponding the reduced thickness of the material, $t_{unsound}$. Assuming that the position of the porosity and the specimen geometry at its location can be established, the difference between the thickness of material that should exist in the specimen at a point and the thickness of material found on the radiograph at a point gives the porosity relative to the sound section of material at the location according to

$$\text{Radiograph} \quad \text{Porosity} \quad \% = \frac{t_{sound} - t_{unsound}}{t_{sound}} \text{ x } 100 \tag{1}$$

This completes Step 4 of the general porosity analysis process.

## Procedures for Radiographic Analysis: Process Details

The details of the analysis include: how data from the radiographs was acquired, how the calibration curve is determined and its accuracy is estimated, how the uncertainty in the porosity measurements from the radiographs is estimated, how the mapping of the specimen geometry on the radiographs is determined (given that they are positioned by hand), and how filtering of the images is performed to remove suspect data and other issues involved in analyzing the radiographs.

A selection of sound material is made so that as large a pool of data as possible can be used to determine the calibration curve of radiograph gray level versus thickness and provide an estimate of the curve's accuracy. For this, the selection of a region of sound material from the digitized radiograph is made using the image analysis program *ImageJ*[16] as shown in Figure 8. The selection of data stored to a file in text format. Three selections of data were taken in this way from each specimen radiograph in the 5 mm diameter test section from: a sound region at the top part of the specimen (above the region with porosity), a sound region at the bottom part of the specimen (below the region with porosity), and a selection from the entire center of the specimen encompassing the length of the specimen and both of the first two regions. Sound section calibration data and specimen position and geometry information was determined for the selections at the top and bottom of the specimen by first averaging the gray level values along the length of the specimen at each across the specimen profile as shown in Figure 8. An example average gray level distribution is shown in Figure 9 with 95% confidence error bars shown. The position data in Figure 9 is expressed in terms of pixel location, rather than specimen center. The specimen center point is determined by trimming the average distribution at the specimen edges, inverting the distribution, and fitting it to a Gaussian distribution function as shown in Figure 10. It is assumed that this center point lies at the vertical center of the selected data, along the specimen length. This process defines the center point of the selected data in pixel units of the specimen radiograph. After this process is performed on the selections from the top and

bottom of the specimen, the centers of those selections can be used to define the specimen centerline, or alignment, as demonstrated for two such distributions. In Figure 11, two example distributions at the top and bottom of the specimen are given, the specimen alignment by the shift of the center points in units of horizontal pixels per vertical pixels can be found and the centerline of the specimen determined. Once the specimen centerline in units of pixels is established, the geometry of the test specimen in the radiograph is referenced to it.

The calibration curve for the sound material is developed using both top and bottom selections of sound data that were used above to define the specimen centerline. The sound thickness is determined from the distance a point lies off of the specimen centerline and the specimen geometry as shown in Figure 12. The 5 mm specimen test section diameter is converted to 0.197 inch, since the radiographs were scanned in 1200 dpi. The dpi of the radiograph was used to convert the distance from the center from pixels to inch. Based on repeated measurements of the entire specimen length for all specimens, a magnification factor was found in the radiographs of approximately 0.5% of the specimen length, and the range in magnification was found to be 0.3% to 0.6%. In no case was the length of the specimen on the radiograph found to be smaller than the real specimen length. Because the magnification was relatively small, it was decided not to correct the dpi in the radiographs. In future analyses this small source of error might be of more concern and could be factored in. Taking the average profile gray level values in the distributions from the top and bottom specimen selections, and their corresponding sound thickness values based on their distance from centerline, a calibration curve of the form

$$\text{Gray Scale Level} = \left(a + b \cdot \text{Thickness}^{c}\right)^{-1} \tag{2}$$

is fit to the data where a, b, and c are unknown coefficients determined by least squares method.

An example curve fit of data for a specimen is shown in Figure 13. The calibration data shown in Figure 13, is very similar in general form to data from all specimens in this study. Several things about this calibration data are apparent from Figure 13: the data becomes more linear at larger thickness values (in this case above approximately 0.15 inches), sensitivity (change in gray scale to change in thickness ratio) goes to zero at low values of thickness, and the limit in thickness detection is approximately 0.08 inches. Given the uncertainty in the average thickness values (as was shown in Figure 9), the standard error of the curve fit in Figure 13, and the loss in sensitivity at smaller thickness values, a cut off thickness must be assigned as shown in Figure 13. Thicknesses of material on the radiograph less than this "minimum detectable thickness" cannot be accurately determined. Figure 14 shows a calibration curve as it would be applied in the radiographic analysis, note that the error bars are not symmetric as the thickness decreases. The confidence interval in Figure 14 is associated with the 95% probability level, as one decreases the probability level the confidence intervals become numerically smaller/tighter for the same calibration data. In Figure 14, the minimum detectable thickness that can be determined from the curve without a value of zero occurring at the lower bound of the confidence interval is approximately 0.07 inches. If one were to decrease the confidence interval probability one would find that a slightly smaller minimum detectable thickness could be obtained. In the present analysis, the confidence interval probability was used in this way to determine the minimum detectable thickness in the radiographs. It was found that this value had

to be varied somewhat (between 80% and 95%) depending primarily on the amount of sound data available in the specimen.

Calibration curves for all "C" specimens in Figure 5 show no systematic variation in calibration curves observed across entire radiograph as shown in Figure 15. Similar results were observed for all specimen families. This indicated there was no discernable non-uniformity of x-rays over the radiograph, or systematic error introduced by the non-uniformity of backlighting in the radiograph re-digitization process. It also indicated that if one specimen in a family of x-rays did not have enough sound material to determine an acceptable calibration curve from, than calibration coefficients from another specimen in the radiograph could be used to analyze that specimen. This only had to be done in the case of three specimens.

Following the generation of the calibration curve and establishing the minimum detectable thickness of material, the selection of the radiograph made of the entire test section of the specimen is analyzed. The value in the numerator of Equation (1), $t_{sound} - t_{unsound}$, is the difference between the section thickness at that point in the specimen if the material were 100% sound and the section thickness that is measured from the radiograph; this difference is termed the "lost section thickness", $t_{lost}$. A comparison between the two radiographic views and the measured lost section thickness from the radiographs for specimen "C" 4 is shown in Figure 16. Note the slight edge effect in the $t_{lost}$ in View 2 of Figure 16 b), this is due to the loss in sensitivity of the calibration curve at very low thickness levels. Generally speaking, the probability value used to create the calibration curve and set the minimum section thickness was adjusted until this effect just vanishes from the plots or is very slight. Applying Equation (1), the porosity can be determined from $t_{lost}$ and the sound/nominal specimen thickness. An example plot of the porosity determined from the radiograph in the specimen is shown in Figure 17. Points in the porosity plot are colored black if they were filtered out of the analysis to demonstrate that filtering occurs primarily at the specimen edges.

At any point along the length of the specimen selection being analyzed, $t_{lost}$ can be summed up across the specimen-cross section to determine the lost area of material at that point along the specimen length, as shown is Figure 18. A cross-sectional porosity fraction can be determined from this lost cross-sectional area by dividing it by the sound/nominal specimen area (5 mm diameter cross section). The resulting comparisons between these results from the radiographs and the fatigue test results will be compared shortly. An example plot of this lost cross-sectional area versus specimen length is shown in Figure 19 and will be discussed in more detail in the next section.

A computer program was written to perform all image calibration and analysis steps using the three input selections from the specimen radiograph (the top, bottom, and entire test section to be analyzed) stored using ImageJ.[16] Input to the computer program include: pixel locations to reference the specimen and specimen selections in the radiograph, the probability parameter for determine the minimum detectable thickness, and calibration coefficients used in the analysis if not automatically determined from the sound data. In all but three specimens the calibration was determined from the specimen being analyzed; in the three cases there was not enough sound data to have a large enough pool of data.

## Results: Fatigue Testing Summary

The fatigue testing results and comparisons with methods of fatigue life calculation are presented in detail elsewhere.[3,13] The test results for all specimens are summarized here as shown in Figure 20. The microporosity specimens had lower fatigue lives than sound keel block specimens[15], and the specimens containing macroporosity had much lower fatigue lives. The fatigue test results for the macroporosity are pertinent to the current analysis so they are summarized in Table 1, which gives: the specimen description, the stress amplitude of the test based on the nominal/sound test section area $S_a$, the fatigue life measured $N_f$, the measured modulus of elasticity for the test specimen from the stable cycle hysteresis loop $E_{meas}$, and the calculated stress amplitude $S_{calc}$ determined from the measured modulus. The calculated stress amplitude is determined assuming that the measured modulus is reduced from the sound modulus because of an increased stress due to the porosity

$$S_{calc} = \frac{S_a \cdot E_{micro}}{E_{meas}} \tag{3}$$

where $E_{micro}$ is the modulus of elasticity measured for the specimens with microporosity in this study (197 GPa). $E_{micro}$ was not found to be much lower than that for the keel block specimens, 207 GPa,[15] but it was decided to use the value from the current studies given that it was taken with recent testing conditions. The calculated stress is used in the plot shown in Figure 20, since it represents the actual stress conditions of the specimens, and these values are repeated in Figure 21 with the scale set to better fit the macroporosity data.

Because monotonic and cyclic material properties are used to compare the fatigue test measurements and radiographs, these properties[3,13] are summarized in Tables 2 and 3, respectively. Monotonic material properties were obtained from two microporosity specimens with the average results shown in Table 2, and are compared to those of the sound specimens.[15] Similar properties for Young's Modulus, E, ultimate tensile strength, $S_u$, and yield strength, $S_y$, found by the 0.2% offset method, were observed, as shown in Table 2. However, the percent reduction of area, %RA, was found to be 75% lower for the microporosity specimens, and neither monotonic microporosity test specimen showed signs of necking. The small values of %RA, and percent elongation, %EL, indicate that the specimens with microporosity had low ductility.

The cyclic and fatigue material properties for the microporosity specimens are compared with the results of the sound specimens[15] as shown in Table 3. The fatigue strength $S_f$ for the specimens with microporosity was found to be 126 MPa, reduced from 297 MPa for sound material. The test data was used to create cyclic σ-ε curve, and a strain versus reversals to failure, ε-$2N_f$, curve. The cyclic stress-strain curve is used to determine material properties which relate the nominal true stress and true strain ranges as given by Equation (4)

$$\Delta e = \frac{\Delta S}{E} + 2\left(\frac{\Delta S}{2K'}\right)^{\frac{1}{n'}} \tag{4}$$

where ΔS and Δe are the nominal true axial stress and true axial strain respectively, E is Young's modulus, K′ is the cyclic strength coefficient, and n′ is the cyclic strain hardening exponent. The value of $S_y'$ was found to be 894 MPa, which is less than $S_y$, indicating that the material cyclic softened. The ε-$2N_f$ curve is composed of the elastic strain amplitude and the plastic strain amplitude curves, and takes the form

$$\frac{\Delta\varepsilon}{2} = \frac{\Delta\varepsilon_e}{2} + \frac{\Delta\varepsilon_p}{2} = \frac{\sigma_f'}{E}(2N_f)^b + \varepsilon_f'(2N_f)^c \tag{5}$$

where Δε/2 ≡ total strain amplitude, $\Delta\varepsilon_e/2$ ≡ elastic strain amplitude, $\Delta\varepsilon_p/2$ ≡ plastic strain amplitude, $\sigma_f'$ ≡ fatigue strength coefficient, b ≡ fatigue strength exponent, $\varepsilon_f'$ ≡ fatigue ductility coefficient, and c ≡ fatigue ductility exponent. The coefficients and exponents for Equation (5) can be found in Table 3 for sound keel block and microporosity data. The plastic strain amplitude curve in Equations (5) is seen to be greatly reduced for the specimens with microporosity, compared to the keel block data.

When modeling pores as "equivalent" notches, the local notch root stress and strain ranges (Δσ and Δε, respectively) can be calculated from the nominal stress ΔS and strain Δe ranges by using Neuber's rule for the case of limited yielding, and by replacing the stress concentration factor $K_t$ with the fatigue notch factor $K_f$

$$\Delta\varepsilon \cdot \Delta\sigma = K_f^2 \Delta e \cdot \Delta S \tag{6}$$

Also, the local notch root stress and strain ranges are used in the equation for the stable cycle hysteresis loop

$$\Delta\varepsilon = \frac{\Delta\sigma}{E} + 2\left(\frac{\Delta\sigma}{2K'}\right)^{\frac{1}{n'}} \tag{7}$$

in applying strain-life concepts to predict fatigue life for components with notches.[17] Since $K_f$ is always less than or equal to $K_t$ in this method, the substitution of $K_f$ for $K_t$ is a conservative assumption.[18] Using the fatigue test specimen data in Tables 1, 2, and 3, Equations (5), (7), and then (6) can be solved to determine an effective $K_f$ for each test specimen; three equations, and three unknowns $K_f$, Δσ, and Δε. Stress concentration factors $K_t$ (and so $K_f$) are defined either with respect to either a gross area, or net section area, as shown in Figure 22. It does not matter which definition is used, provided the correct nominal area (gross or net section area) is used to define the nominal stress, and one is consistent. In the presentation of the results that follow, $K_f$ is determined for each specimen test using the measured modulus. Use of the measured modulus provides a greater value for the elastic strain amplitude than if the $E_{micro}$ were used, and it a higher value is reflective of the strain amplitude Δe measured in the test. Since the measured modulus E is based on the measured strain and the gross section stress applied to a specimen, the resulting $K_f$-porosity relationship might prove useful in applying the method to components, where the gross section areas and stresses would be readily available from analysis, and where the porosity field in the part would determine the elastic modulus distribution. The calculation of $K_f$ begins with using Equation (5) to calculate the total strain amplitude given a specimen's life $N_f$, modulus E, and fatigue properties. Equation (7) is solved next using the measured modulus and hysteresis loop properties data to determine Δσ. The nominal gross section specimen area and stress are used in Equation (6) to determine $K_f$. This method is used here to demonstrate one

method how the results from the fatigue tests may be used to determine the fatigue notch factor for the test specimens. Other methods to accomplish this are being explored as well.

A porosity percentage is calculated from the measured elastic modulus, $E_{meas}$, of each specimen according to

$$\text{Elastic Modulus - Based Porosity\%} = 100\left(1 - \frac{E_{meas}}{E_{micro}}\right) \quad (9)$$

where the constant $E_{micro}$ is the modulus of the specimens with microporosity. This porosity may also be converted into a lost sectional area in the specimen as shown in Figure 19 by taking it as a percentage of the nominal specimen area. The measured cross-sectional porosity, and the area of porosity (or lost sectional area), from the radiographs will be compared with that from the measured modulus in the next section.

## Results: Comparison of Fatigue Testing and Radiographic Analysis

In order the check the accuracy of the radiograph measurements, a scanning electron microscope (SEM) was used to make an image of a cut and polished surface of a specimen, E5, as shown in Figure 23. The position of this surface along the specimen length was known and its position determined in the radiographs. At this length position, measurements of the lost thickness from a radiographic analysis across the diameter of the specimen using the method described earlier were compared with handmade measurements of lost thickness from the cut surface. The handmade measurements were performed by adding up the total length of voids occurring along a path through the specimen across the specimen diameter. Since two radiographic views were taken, two comparisons with the cut surface measurements are made. Figure 24 and Figure 25 show the comparisons for the views, 1 and 2, respectively. The comparisons are good, and the agreement between the surface and radiograph are within the error of the radiographic analysis. Overall, the measurements from the cut surface appear to be lower than the radiographic analysis; this might be because very small indications on the cut surface were difficult to interpret and were not included in the surface measurements. Also, since the orientation of the radiographic views was only approximately known, there may be a shift in some of the features seen on the surface. The agreement between the two is acceptable as a check on the radiographic analysis.

As discussed earlier, the lost cross-sectional area (or cross-sectional area of porosity) along the length of the specimen test section can be determined from the radiographs. In Figure 19, such results from the two radiographic views are shown and are compared with the lost cross-sectional area determined from the measured modulus, which is determined by multiplying the porosity fraction from Equation (9) times the sound specimen cross-sectional area. The sound specimen cross-sectional area is 0.0304 $in^2$ (19.6 $mm^2$) at the test section. Notice in Figure 19 that the maximum lost cross-sectional area along the specimen length corresponds well to the lost cross-sectional area determined from the measures specimen modulus. Not too surprisingly, this indicates that the dominant feature affecting the measured elastic modulus of the specimens is the cross-section with the least area (most porosity). Note the agreement between the measurements from both radiographic views. This indicates that the repeatability of this measurement from the radiographs is quite good. Comparisons between the lost area from

the radiographs and the value derived from the measured modulus are compared for eleven more specimens in Figures 26 and 27. In Figure 26, six "least" macroporosity specimen are shown, and the probability parameter used to filter the data and set the minimum detectable thickness is shown. In figure 26 a), note that the effect of varying the probability parameter for specimen "C2" View 1 from 50%, to 85%, to 95%, does not affect the cross-sectional area measurement, and that both views agree well with the result from the measured modulus. For all specimens shown in Figure 26, the agreement between the lost cross-sectional area in the two radiographic views is good, and the maximum lost cross-sectional area agrees best with the results from the measured elastic modulus. In Figure 27, results for a specimen family with the "most" macroporosity ("D") is shown, and the agreement between the lost area determined from the measured modulus and maximum lost area from the radiographic analysis is even better than Figure 26. Note in Figure 27 b), that the probability level for specimen D5 View 2 is varied from 60%, to 80%, to 85%, in order to show how it affects the results. This demonstrates that it may be necessary to vary this parameter in the analysis from radiograph to radiograph to capture important features. Having two radiographic views serves as a good check on the analysis.

The lost cross-sectional area determined from the radiographs is used to calculate a cross-sectional porosity by dividing it by the area of the specimen test section. This maximum cross-sectional porosity occurring in the radiographs versus the specimen porosity determined from the elastic modulus is plotted in Figure 28. The error of the porosity measurement from the radiographs is estimated to be ±4.6% porosity. This is a conservative estimate based on the total error from the calibration process and repeatability between radiographic views. Bars representing this error band are included in Figure 28 for the radiographic measurements. Considering the line of one-to-one correspondence, there is quite good agreement between the two in Figure 28. That is not to say that this was expected; it is just an observation. There is also a tendency for the radiographic measurements to be less than the modulus derived values, especially at lower values of porosity. If a one-to-one correspondence between the two should exist, this observed trend might be due to "missing" porosity not detected in the radiographs due to the low sensitivity of the radiographs to thin sections of material.

The measured elastic modulus $E_{meas}$ and the maximum cross-sectional porosity for each specimen are plotted in Figure 29. In this plot there are microporosity specimens as well, for comparison. The sound elastic modulus for 8630 steel is 207 GPa, and the specimens with microporosity measured in this study were found to be 197 GPa on average. Note that there is a strong trend of decreasing $E_{meas}$ with increasing maximum cross-sectional porosity in the radiographs. A best fit for the macroporosity data using a power law gave an exponent of 1.17, so the data is quite linear. A linear fit of the macroporosity data passes through a zero porosity value significantly below the sound property value. Additional test specimens with less porosity, to fill in the region from 5% to 15% porosity might provide more insight here. Also there is a substantial difference in the maximum porosity level and $E_{meas}$ between the "most" macroporosity specimens and those of having "least" and "middle" geometry. In fact, the "middle" geometry specimens appear to have least porosity here, and have the highest modulus of all the macroporosity specimens. At the same time, two of the "middle" specimens have the lowest $E_{meas}$ values despite having lower maximum cross-section porosity values than a number of the "least" specimens. Overall, one can say that the "least" and "middle" specimens have very

similar ranges of $E_{meas}$ and maximum cross-sectional porosity, and they had similar fatigue life characteristics as well.

After using of Equations (5), (6), and (7) and the fatigue test data to determine the gross section fatigue notch factor $K_f$, the resulting $K_f$ values are plotted in Figure 30 versus the maximum cross-section porosity determined from the radiographs. The data appears to correlate well, leading one to ask whether this data could be used in a general way for a component with some know internal porosity. Unfortunately, any correlation using the data would only be applicable to porosity in a round bar with applied tension, with the porosity being of similar scale as the bar. So, the results are geometry specific as presented in Figure 30; there is a specimen size effect in the data that would make it not applicable directly in a general case. Nevertheless, the data provides insight and may be used to test general models, and it indicates a relationship between $K_f$ and porosity.

Considering the results shown in Figure 30, some preliminary results were prepared to show 1) whether the $K_f$ in Figure 30 make physical sense compared to handbook values, and 2) whether is it possible to non-dimensionalize the results and remove the effect of the specimen size and present the results in a general way. The handbook of stress concentration factors[5] was consulted to investigate how these results compare with textbook stress concentration factors. Unfortunately, comparing the results to the Neuber notch and other ellipsoidal notch factors that were used in a previous study[3] was not successful. Considering these are applicable to infinite bodies, this is not surprising. Encouraging, preliminary, comparisons are made looking at stress concentrations for finite bodies, round bars with transverse and spherical holes. The stress concentration factors for these bars depend upon the hole-to-bar diameter ratio (d/D). Simplifying the maximum cross-sectional porosity as an area ratio (porosity area to cross-sectional specimen area ratio), an equivalent diameter ratio for the porosity can be calculated by taking the square root of the porosity ratio

$$\sqrt{\text{Porosity Fraction}} = \sqrt{\frac{A_{porosity}}{A_{specimen}}} = \frac{d_{porosity}}{D_{specimen}} \tag{10}$$

where $d_{porosity}$ is the equivalent porosity diameter and $D_{specimen}$ is the specimen diameter. As a first effort at comparison, this is fine, but the porosity is not a circle. Using Equation (10) allows for a ready comparison given the data in hand. The comparison between the handbook stress concentration factors (gross area) and the fatigue notch factors from the fatigue testing is shown in Figure 31 (noting that $K_f \leq K_t$). Using the equivalent porosity diameter to specimen diameter ratio (square root of maximum cross-sectional porosity fraction from the radiographs) the plot shows that the fatigue notch factors from the tests fall between the relationship for a transverse hole in a round bar and a spherical hole in a bar (both of diameter d/D). Furthermore, for the case of the transverse hole in the bar, if the bar is changed to a tube like in many of the most porous specimens, the $K_t$ curves move down toward the fatigue test data with increasing tube diameter. In any event, the fatigue test data analyzed in this way appear to have a correspondence to similar handbook stress concentration cases. This is the subject of ongoing investigation. Further analysis, compiling the data for the dimensions of the porosity using the lost thickness measurements of the two radiographic views, and comparing them with the handbook cases, and possibly developing a correlation, are underway. These investigations are

being conducted with the ultimate goal in mind, how to apply the fatigue calculations to porosity in a general way.

## Summary and Conclusions

A method for measuring porosity from radiographs of fatigue test specimens taken prior to fatigue testing has been presented. A procedure for using the specimens themselves to perform an in situ calibration for the measurements is described, where the accuracy of the measurements can be established. Measured porosity dimensions from the radiographs were found to agree well with measurements made on a cut and polished specimen surface. The specimen porosity measurements are summed up over the specimen cross sections to determine the cross-sectional porosity versus length distribution along the specimens. The accuracy of this cross-sectional measurement is conservatively estimated to be 4.6% porosity. Cross-sectional porosity distributions determined from two radiographic views of the specimens show excellent agreement, and demonstrate the method's repeatability. The maximum cross-sectional porosity in the radiographs was found to correlate well with the fatigue test specimens' measured elastic modulus. Converting the elastic modulus measurements to an apparent porosity in the specimen, a close one-to-one correspondence was found between this and the maximum cross-sectional porosity in the specimens. The average specimen porosity determined from the radiographs did not correlate with the measured elastic modulus. The maximum cross-sectional porosity found in the specimens in this study ranged from about 15% to 65% based on the radiographic analysis.

Fatigue test results were compared with the radiographic analysis by determining the fatigue notch factors of the test specimens based on their measured fatigue lives, test conditions, measured elastic modulus and other properties. Comparisons between the notch factor and porosity from the radiographs showed a good correlation, but this result is specific to the test geometry used. Using an equivalent porosity to specimen diameter ratio, comparison with textbook stress concentration factors showed the results to be quite plausible, somewhere between the effect of a transverse hole and a spherical hole in a round bar. This comparison was performed as a preliminary effort to explain the effect of the porosity size on fatigue, and to see if the fatigue test results were meaningful in the context of handbook values. It is also a first attempt to account for the relative sizes of the specimen and porosity in the test results, to non-dimensionalize the results, and to make the results more generally applicable. Work on this, using the actual dimensions of porosity measured from the radiographs, is currently in progress.

Radiographic analysis is ongoing, investigating the porosity dimensions and correlating them to fatigue notch factors. Explaining scatter in the fatigue test data through analysis of the porosity dimensions, and transferring that to a general model (rather than geometry specific model) of fatigue behavior remains the ultimate goal. Efforts are also underway to reconstruct the specimen porosity from the radiographs and input them to finite element simulations of the test specimen. This is being done to test general models being developed to predict the performance of cast steel with porosity. Centrifugally and statically (trapezoidal) cast 8630 steel specimens are currently undergoing fatigue testing. New fatigue test specimens are being cast at Southern Cast Products which are designed to result in lower levels of macroporosity than the data discussed here. Also, these specimens will have larger cross-sectional area. This should

provide additional data below the 15% porosity level, and data for which the specimen size may not play as dominant a role in determining the fatigue behavior.

## Acknowledgments

This research was undertaken as part of the Integrated Design of Steel Castings for Service Performance project which is funded by the United States Department of Defense through the American Metalcasting Consortium (AMC) PRO-ACT program. AMC's PRO-ACT program is sponsored by Defense Supply Center Philadelphia (DSC, Philadelphia, PA) and the Defense Logistics Agency (DLA, Ft. Belvoir, VA). This research is also conducted under the auspices of the Steel Founders' Society of America, and through substantial in-kind support, guidance and interest from SFSA member foundries. In particular, we would like to thank Harrison Steel for several trial iterations of test specimens and the final test specimen castings, Alloy Weld Inspection Co. for their digital and film radiography of the fatigue test specimens, Southern Cast Products for their willingness to create a new test specimen casting pattern and to cast new test specimens, and MAGMA GmbH for their support of the porosity prediction model used to design the test specimen castings. Any opinions, findings, conclusions, or recommendations expressed herein are those of the authors and do not necessarily reflect the views of DSC, DLA, or the SFSA and any of its member foundries.

## References

1. E.K. Weber, and G.B. Raab, "Fatigue in Steel Castings Design Considerations," in Proceedings of the 52nd Technical and Operating Conference, SFSA, Chicago (1998).

2. K.D. Carlson, Z. Lin, R.A. Hardin, C. Beckermann, G. Mazurkevich and M.C. Schneider, "Modeling of Porosity Formation and Feeding Flow in Steel Casting", *Proceedings of Modeling of Casting, Welding and Advanced Solidification Processes X*, (May 25-30, Destin, Florida, 2003), 295-302.

3. Sigl, K.M., Hardin, R., Stephens, R.I., and Beckermann, C., "Fatigue of 8630 Cast Steel in the Presence of Shrinkage Porosity," in Proceedings of the 57th Technical and Operating Conference, SFSA, Chicago (2003).

4. R. I. Stephens, A. Fatemi, R. R. Stephens, H. O. Fuchs, *Metal Fatigue in Engineering* (2nd Edition, Wiley-Interscience, New York, 2000).

5. R. E. Peterson, *Stress Concentration Factors* (Wiley-Interscience, New York, 1974), p. 137.

6. R. E. Peterson, "The Interaction Effect of Neighboring Holes or Cavities, With Particular Reference to Pressure Vessels and Rocket Cases", *Transactions of the ASME Journal of Basic Engineering*, 1965, **87(4)**, pp. 879-886.

7. H. Greenberg, "An Engineering Basis for Establishing Radiographic Acceptance Standards for Porosity in Steel Weldments", *Transactions of the ASME Journal of Basic Engineering*, 1965, **87(4)**, pp. 887-893.

8. P. Heuler, C. Berger, J. Motz, "Fatigue Behaviour of Steel Castings Containing Near-Surface Defects", *Fatigue & Fracture of Engineering Materials & Structures*, 1992, **16(1)**, pp. 115-136.

9. M.F. Horstemeyer, "Mapping Failure by Microstructure-Property Modeling", *Journal of Metals*, 2001, Sept., pp. 24-27.

10. M.F. Horstemeyer, R.J. Osborne, and D.E. Penrod, "Microstructure-Property Analysis and Optimization of Control Arm", *AFS Trans.*, 2002, 02-036, pp. 1-18.

11. D.L. McDowell, K. Gall, M.F. Horstemeyer, and J. Fan, "Microstructure-Based Fatigue Modeling of Cast A356-T6 Alloy", *Engineering Fracture Mechanics*, 2003, **70(1)**, pp. 49-80.

12. M.F. Horstemeyer, N. Yang, K. Gall, D.L. McDowell, J. Fan, and P.M. Gullett, "High Cycle Fatigue of a Die Cast AZ91E-T4 Magnesium Alloy", *Acta Materialia*, 2004, **52(5)**, pp. 1327-1336.

13. K.M. Sigl, R. Hardin, R.I. Stephens, and C. Beckermann, "Fatigue of 8630 Cast Steel in the Presence of Porosity," *International Journal of Cast Metals Research*, 2004, 17(3), pp. 130-146.

14. Standard E606, "Standard Practice for Strain-Controlled Fatigue Testing", *2002 Annual Book of ASTM Standards* (American Society of Testing and Materials, West Conshohocken, PA 2002), **Vol. 03.01**, pp. 569-583.

15. R. I. Stephens, *Fatigue and Fracture Toughness of Five Carbon or Low Alloy Cast Steels at Room or Low Climatic Temperatures* (Carbon and Low Alloy Technical Research Committee, Steel Founders' Society of America, Des Plaines, IL, 1982).

16. ImageJ 1.32j, Wayne Rasband, National Institutes of Health, USA.

17. J.A. Bannantine, J.J. Comer, and J.L. Handrock, *Fundamentals of Metal Fatigue Analysis*, (Prentice-Hall, New Jersey, 1990), pp.124-156.

18. T.H. Topper, R.M. Wetzel, and J. Morrow, "Neuber's Rule Applied to Fatigue of Notched Specimens", *Journal of Materials*, 1969, 4(1), pp. 200-209.

Table 1 – Macroporosity Specimen Load Control Test Data and Results

| Specimen ID | Porosity Level | Stress Amp (MPa) | $N_f$ | E (GPa) | Calculated Stress (MPa) |
|---|---|---|---|---|---|
| C4 | Least | 126 | 24 320 | 143 | 174 |
| C8 | Least | 126 | 29 023 | 153 | 163 |
| C2 | Least | 96 | 1 365 | 137 | 138 |
| C3 | Least | 96 | 79 908 | 149 | 127 |
| C9 | Least | 66 | 216 516 | 145 | 90 |
| C10 | Least | 66 | 4 053 800 | 141 | 92 |
| C5 | Least | 53 | 851 275 | 138 | 76 |
| H8 | Middle | 126 | 7 456 | 148 | 168 |
| 5 | Middle | 126 | 13 013 | 142 | 175 |
| H3 | Middle | 126 | 40 896 | 155 | 161 |
| G2 | Middle | 96 | 4 392 | 111 | 171 |
| G8 | Middle | 96 | 41 066 | 125 | 152 |
| H7 | Middle | 96 | 333 025 | 142 | 134 |
| H2 | Middle | 66 | 769 074 | 151 | 86 |
| G1 | Middle | 66 | 1 681 018 | 166 | 79 |
| G7 | Middle | 53 | 249 752 | 143 | 73 |
| G4 | Middle | 53 | 1 342 218 | 145 | 72 |
| E6 | Most | 126 | 160 | 120 | 207 |
| E8 | Most | 126 | 11 648 | 136 | 183 |
| D6 | Most | 126 | 37 089 | 135 | 184 |
| E1 | Most | 96 | 1 935 | 90 | 211 |
| E5 | Most | 96 | 6 042 | 77 | 246 |
| D10 | Most | 66 | 15 419 | 113 | 115 |
| D4 | Most | 66 | 57 566 | 135 | 97 |
| D8 | Most | 66 | 113 503 | 136 | 96 |
| D5 | Most | 53 | 10 812 | 87 | 120 |
| E10 | Most | 53 | 15 868 | 104 | 101 |

Table 2 - 8630 Steel Monotonic Properties

| Property | Micropore Material Avg. | Sound Material[15] |
|---|---|---|
| $S_u$ (MPa) | 1 125 | 1 144 |
| $S_y$ (MPa) | 1 088 | 985 |
| E (GPa) | 197 | 207 |
| %EL | 2.5 | ---- |
| %RA | 7.0 | 29 |
| $\sigma_f$ (MPa) | 1 156 | 1 268 |
| $\varepsilon_f$ | .073 | .35 |
| K (MPa) | 1 307[#] | ---- |
| N | .0279[#] | ---- |

[#] Not the arithmetic mean but the best fit regression to the aggregate data

Table 3 - 8630 Steel Cyclic Properties

| Property | Micropore Material | Sound Material[15] |
|---|---|---|
| $S_f$ (MPa) | 126 | 293 |
| $S_f/S_u$ | .11 | .26 |
| K′ (MPa) | 2 550* | 1 502 / 2 267[#] |
| n′ | .167* | .122 / .195[#] |
| $S_y'$ (MPa) | 894* | 682 / 661[#] |
| b | -.176 | -.121 |
| c | -.908 | -.693 |
| $\sigma_f'$ (MPa) | 2 390 | 1 936 |
| $\varepsilon_f'$ | .11 | .42 |

* Data determined from the companion method

[#] Data determined from the companion and incremental step methods respectively

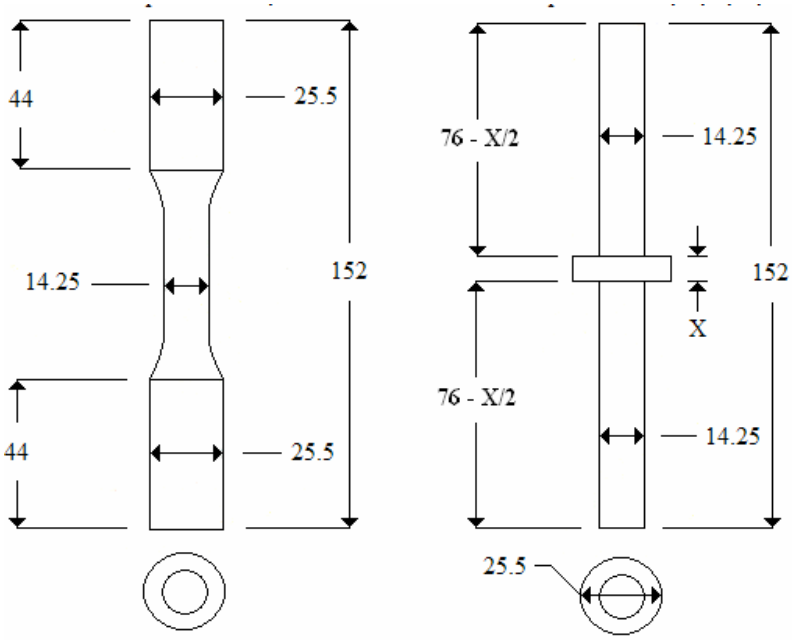


(a) Microporosity Specimen Blanks (b) Macroporosity Specimen Blanks

Figure 1 - Dimensions of cast blanks in millimeters. Dimension "X" = 5, 7.5, and 10 mm for the "least", "middle", and "most" macroporosity specimen groups respectively.

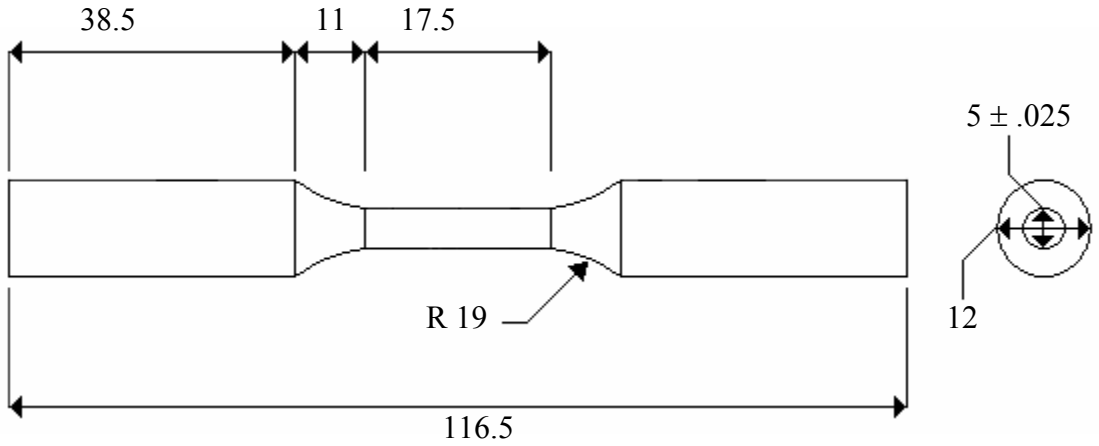


Figure 2 - Final dimensions of fatigue specimens in millimeters

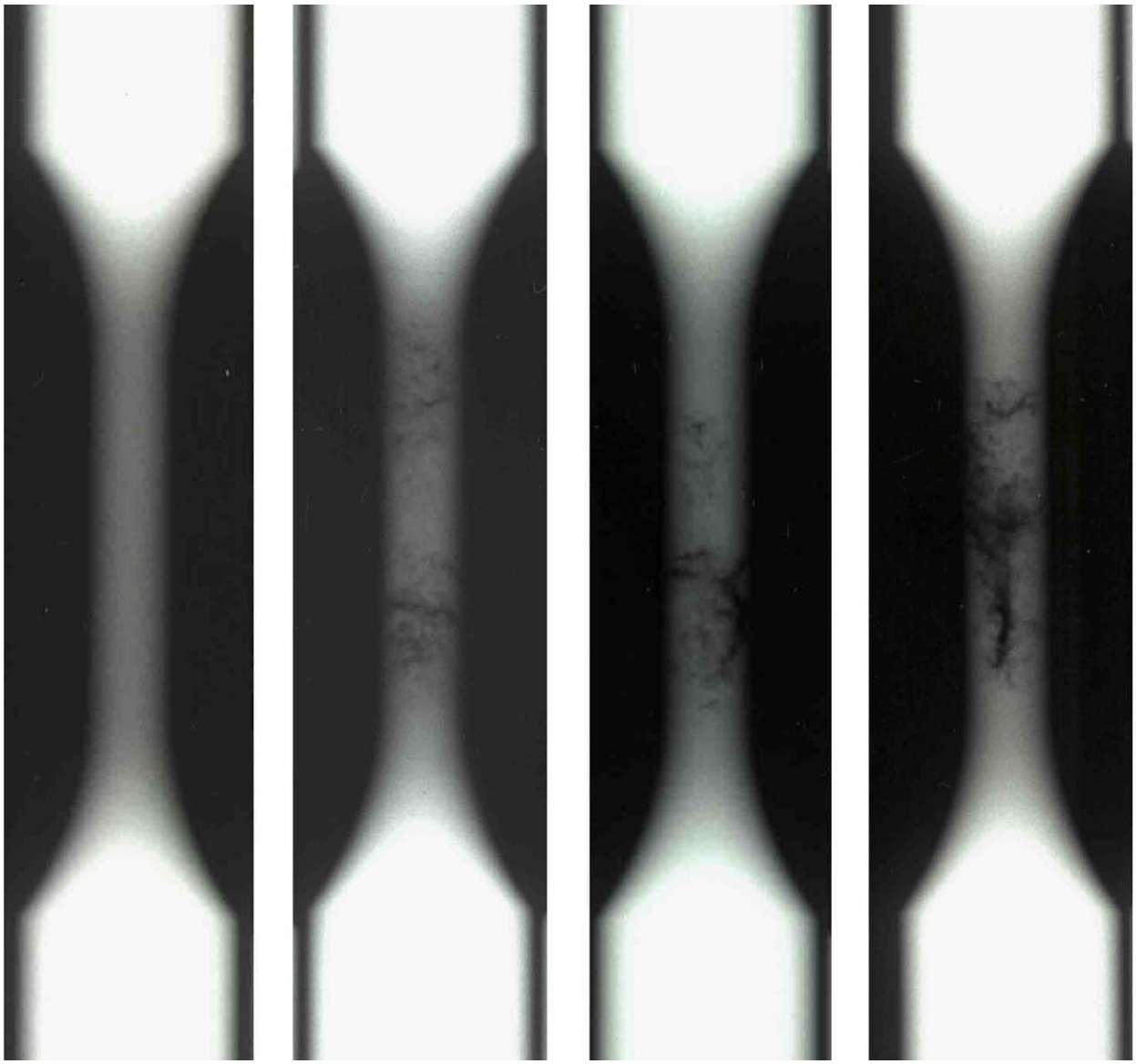

(a) (b) (c) (d)

Figure 3 – Examples of specimen radiographs for the range of porosity present in the fatigue test specimens (a) microporosity, (b), (c), and (d) are “least”, “middle”, and “most” specimens with macroporosity, respectively.

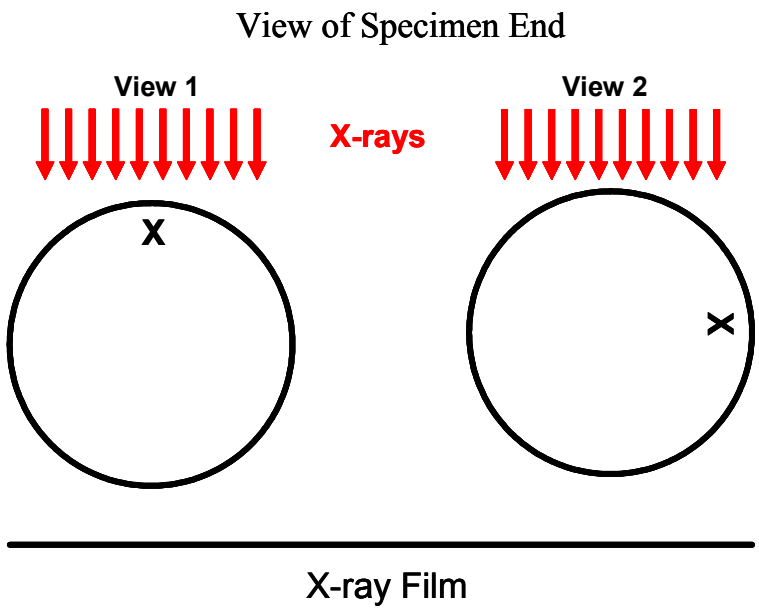


Figure 4 – End view of specimen orientation for the two orthogonal radiographs taken of each specimen family

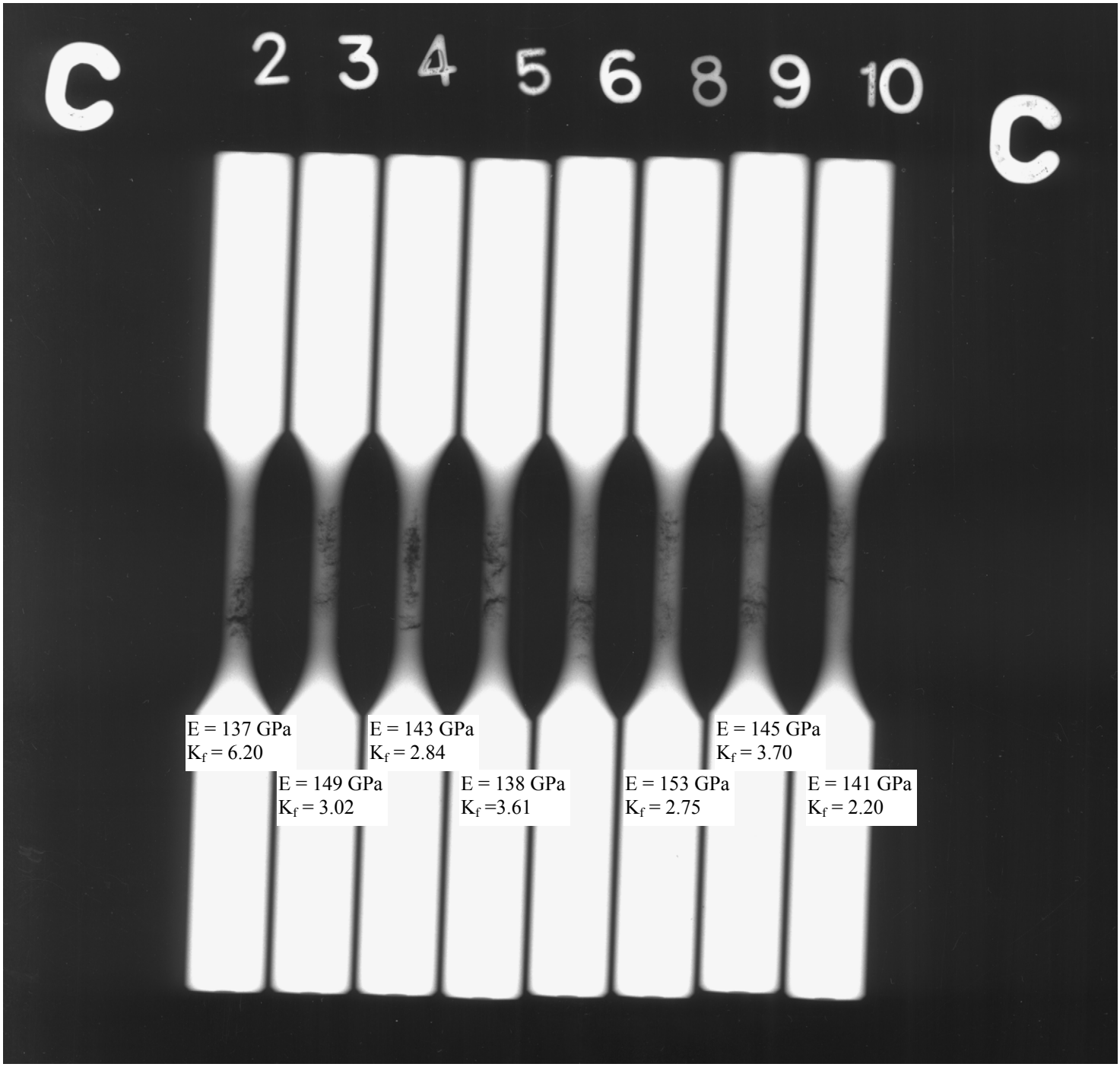


Figure 5 – View #1 of the two orthogonal radiographic views of specimen family "C"

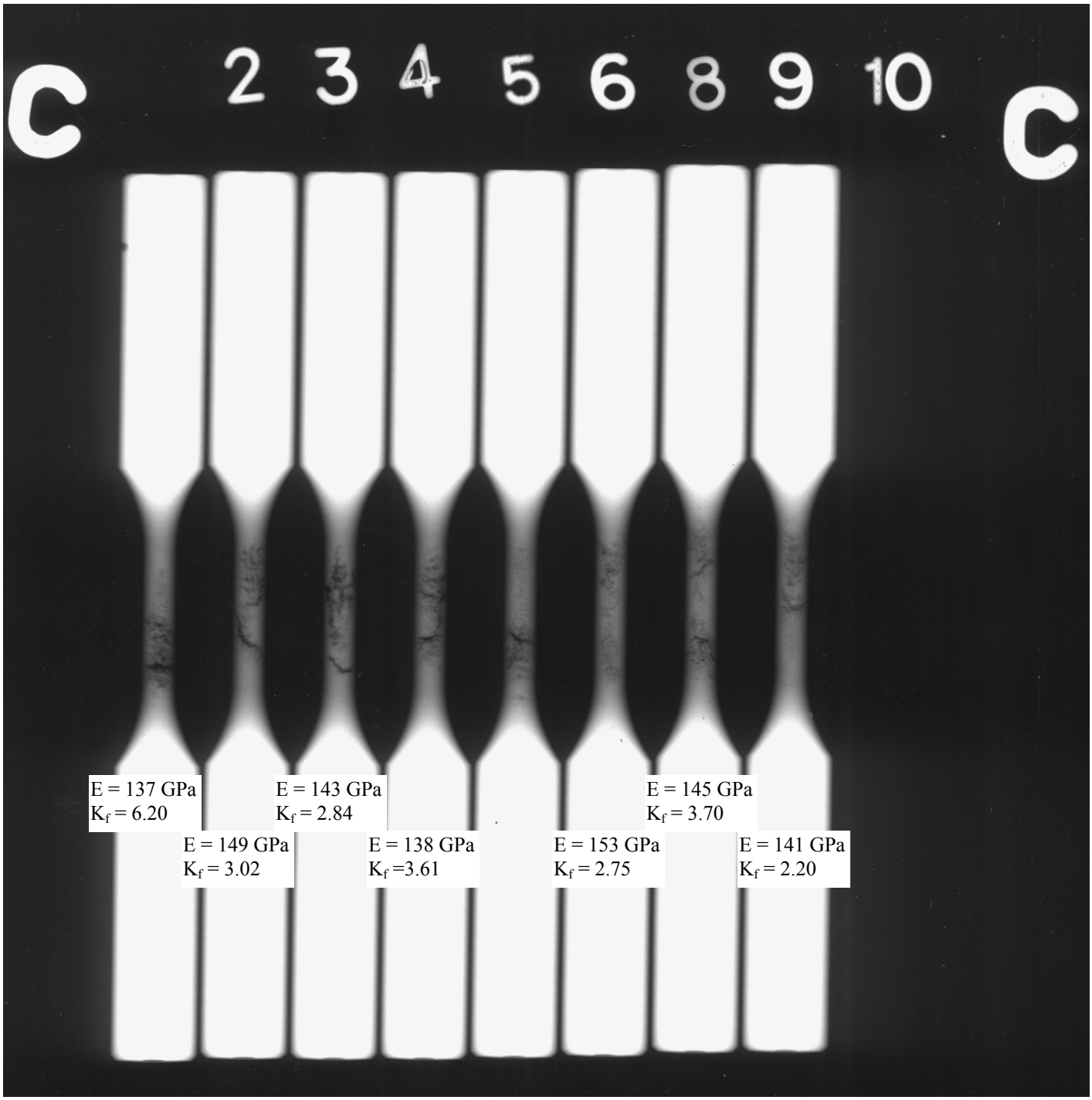


Figure 6 – View #2 of the two orthogonal radiographic views of specimen family "C"

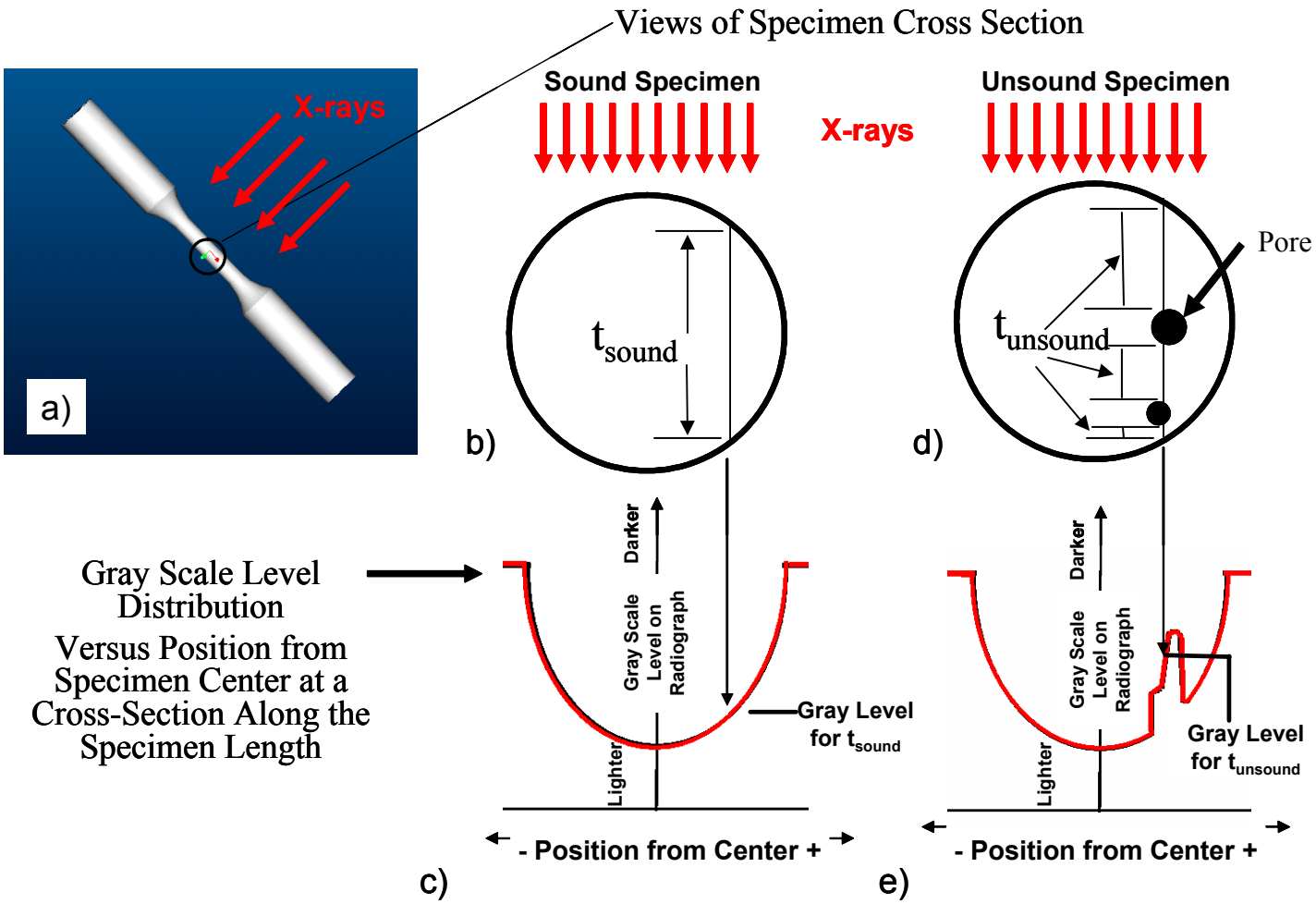


Figure 7 – a) full test specimen and incident x-rays, center test section with circular cross-section to be analyzed is circled, b) incident x-rays on a sound specimen cross-section, and an example x-ray path through the specimen and the corresponding thickness of material to $t_{sound}$, c) gray level distribution for a sound specimen (shown in red) versus position across specimen relative to specimen center, the gray level corresponding to $t_{sound}$ is indicated, gray level is greater/darker as the thickness decreases, d) an unsound test section with x-ray path and corresponding total thickness of material $t_{unsound}$, e) gray level distribution for a specimen with porosity.

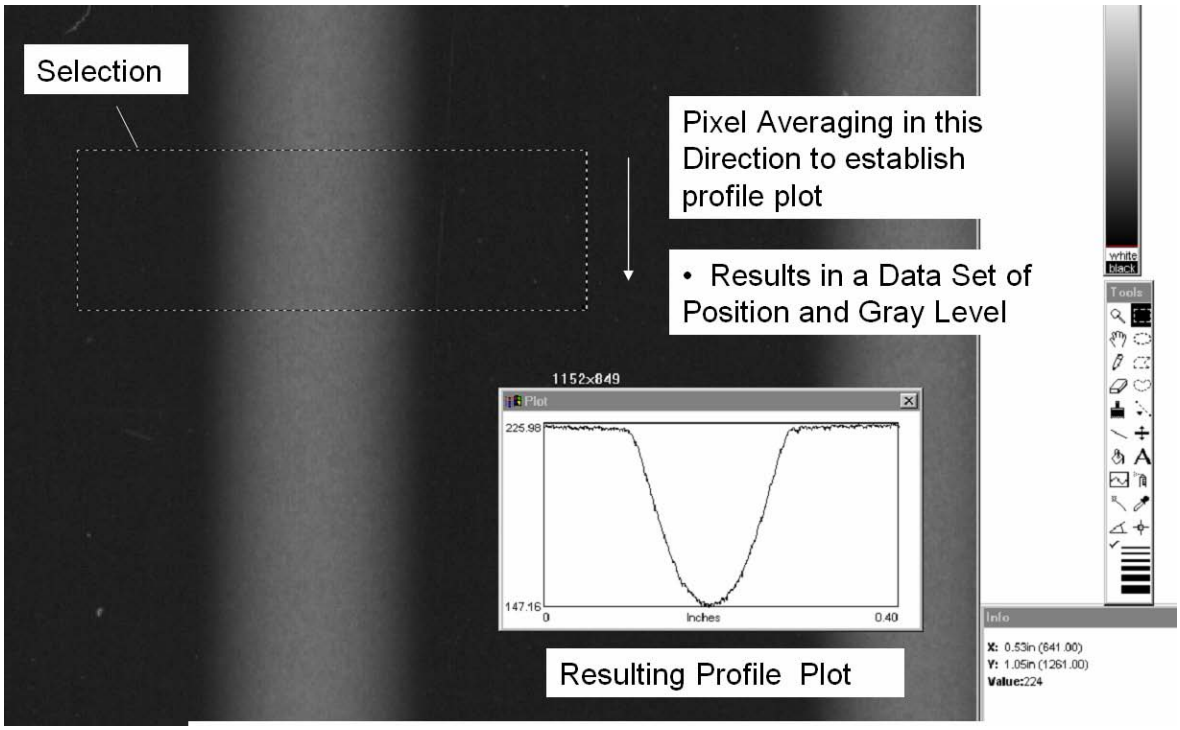


Figure 8 – Example selection of sound specimen radiographic data, and averaged gray level "Resulting Profile Plot" across specimen section.

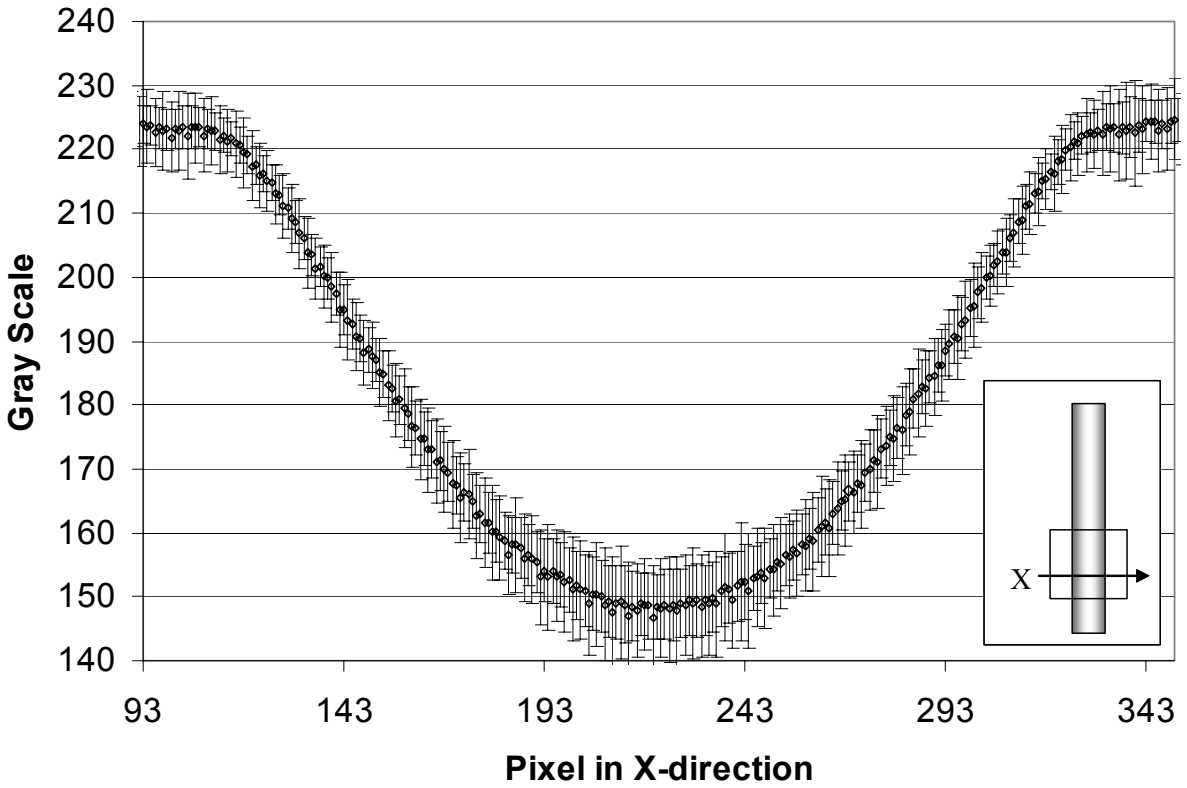


Figure 9 – Plot of the average gray level (or gray scale reading) and error bars based on 95% confidence across the selection of the specimen section shown in Figure 8.

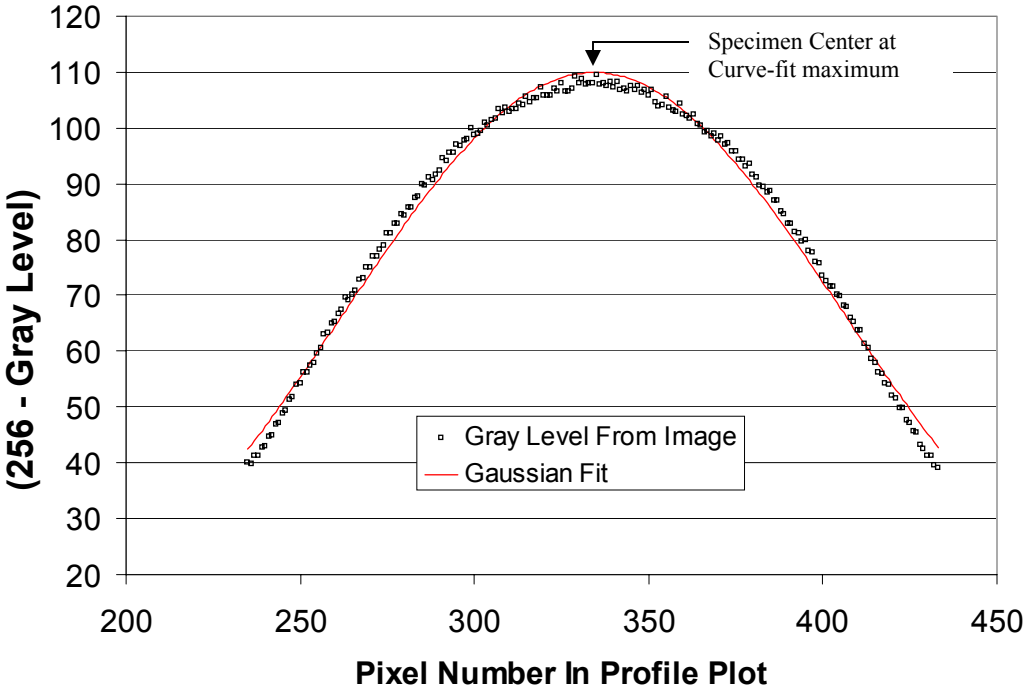


Figure10 – Conversion of the average gray level distribution to a form that can be fitted to a Gaussian distribution for determining the specimen center, and an example fit used to determine specimen center.

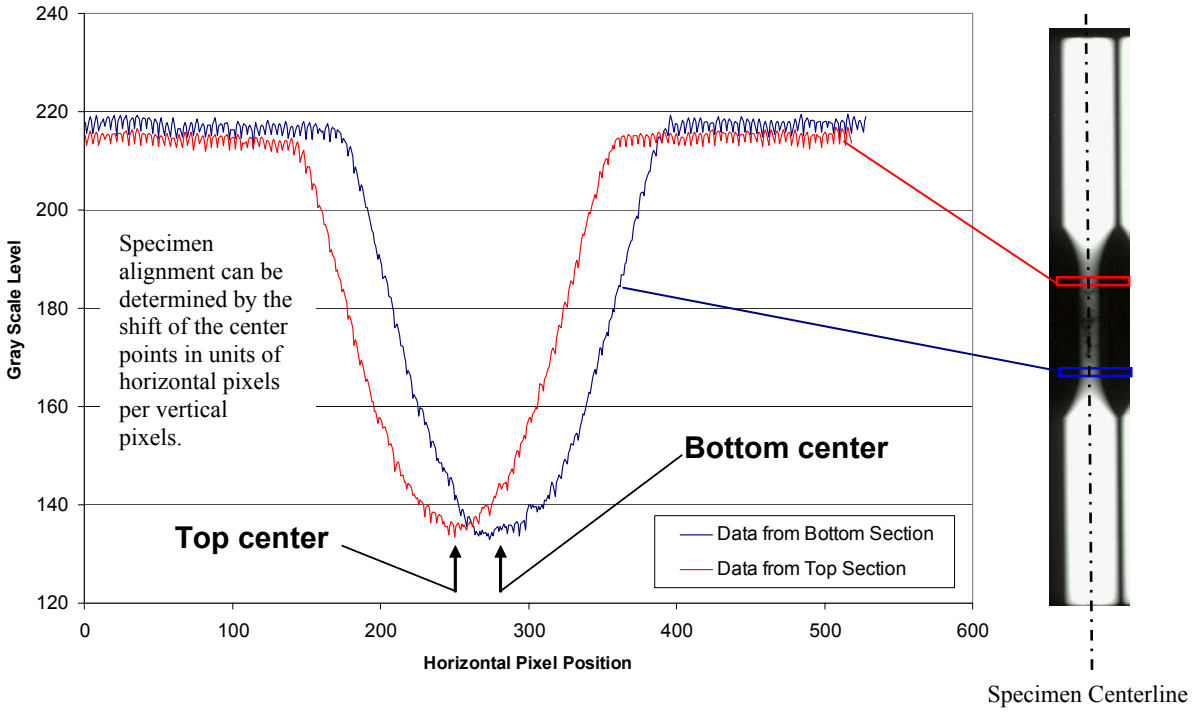


Figure 11 – Distributions across specimen at the top and bottom sections, offset of the specimen centers is determined and used to correct for specimen alignment.

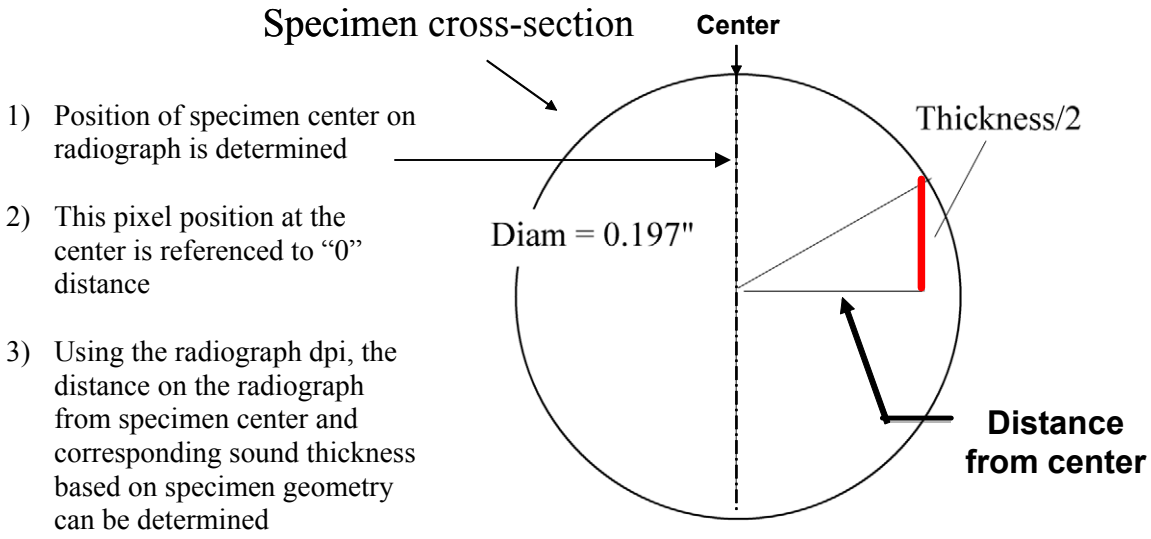


Figure 12 – Determination of specimen geometry and thickness distribution, end view of specimen cross section.

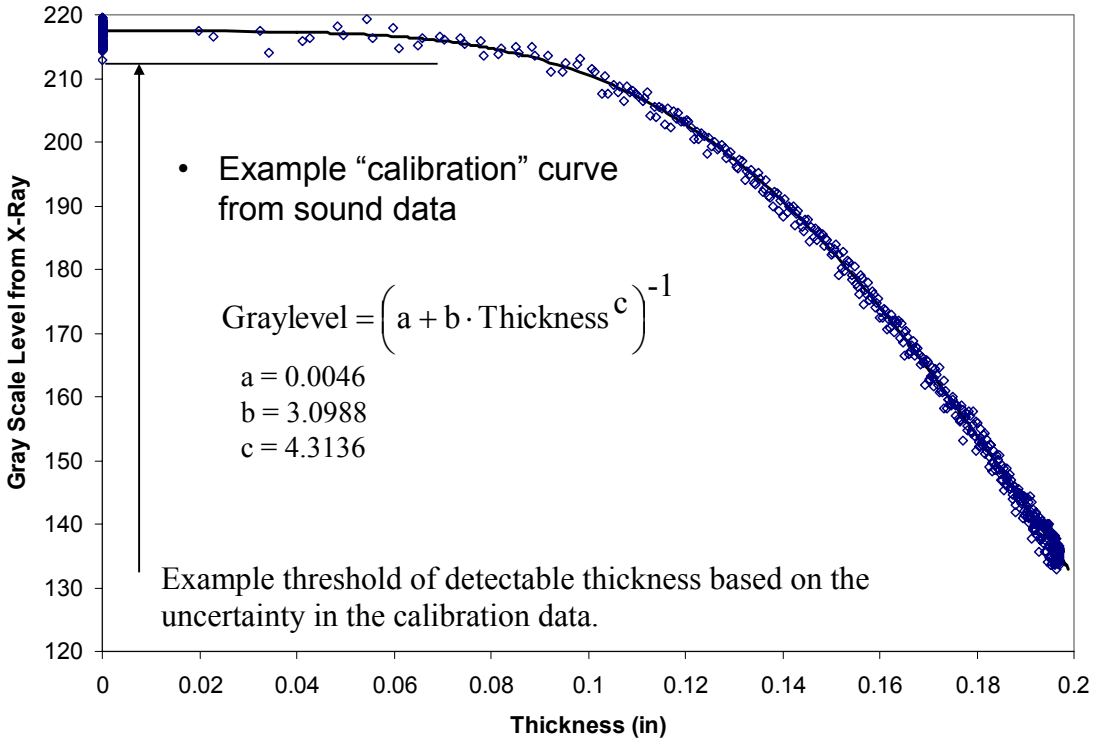


Figure 13 – Example calibration curve from distribution of sound data.

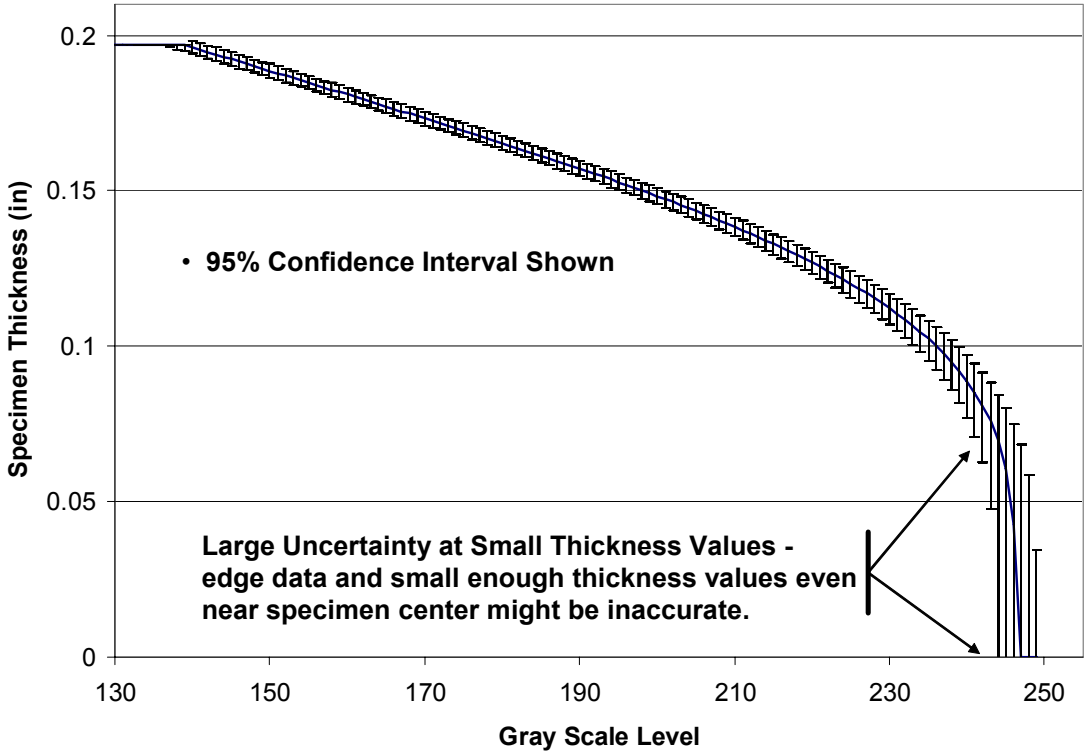


Figure 14 – Calibration curve as applied to determine specimen thickness (output) from gray scale level in radiograph, note that uncertainty bars are not symmetric due to the loss in sensitivity.

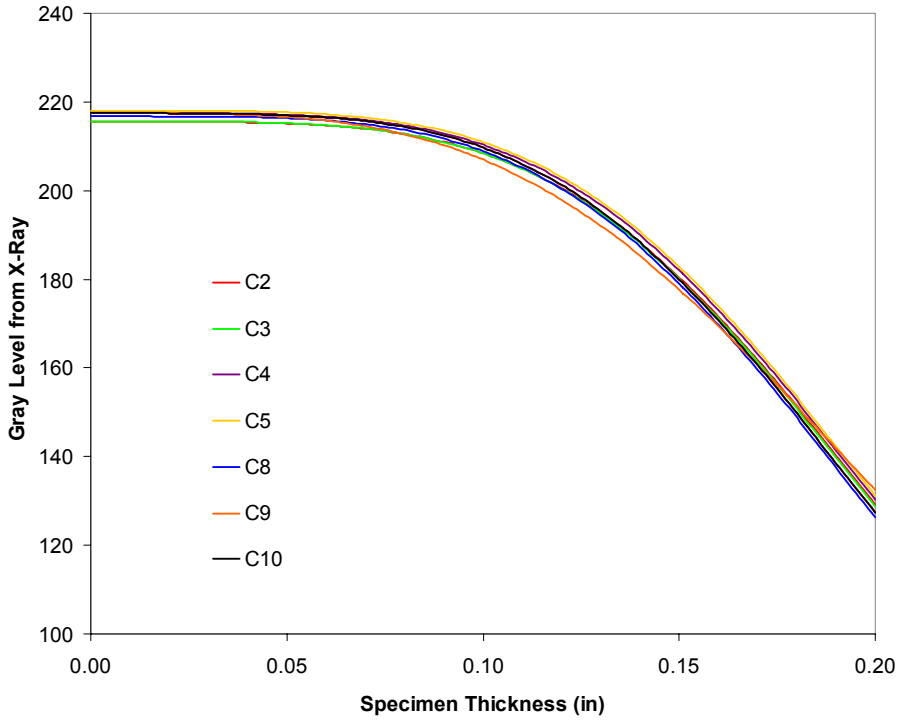


Figure 15 – Calibration curves for all specimens in Figure 5, no systematic variation in calibration curves is observed across the entire radiograph of family “C” specimens.

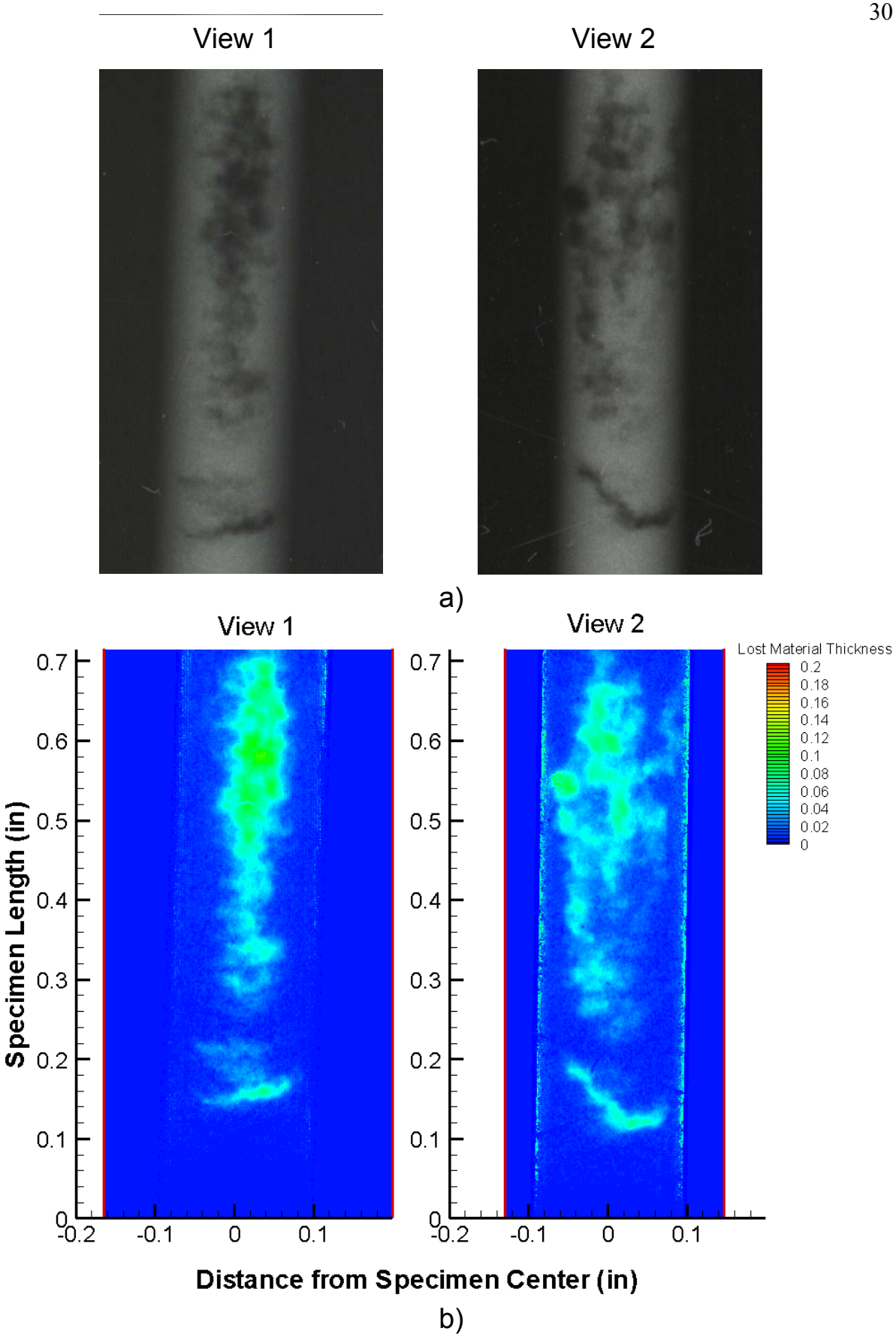


Figure 16 – Comparison between a) radiographs and b) lost material thickness measured from the radiographs for specimen "C" 4, both orthogonal radiographic views are shown.

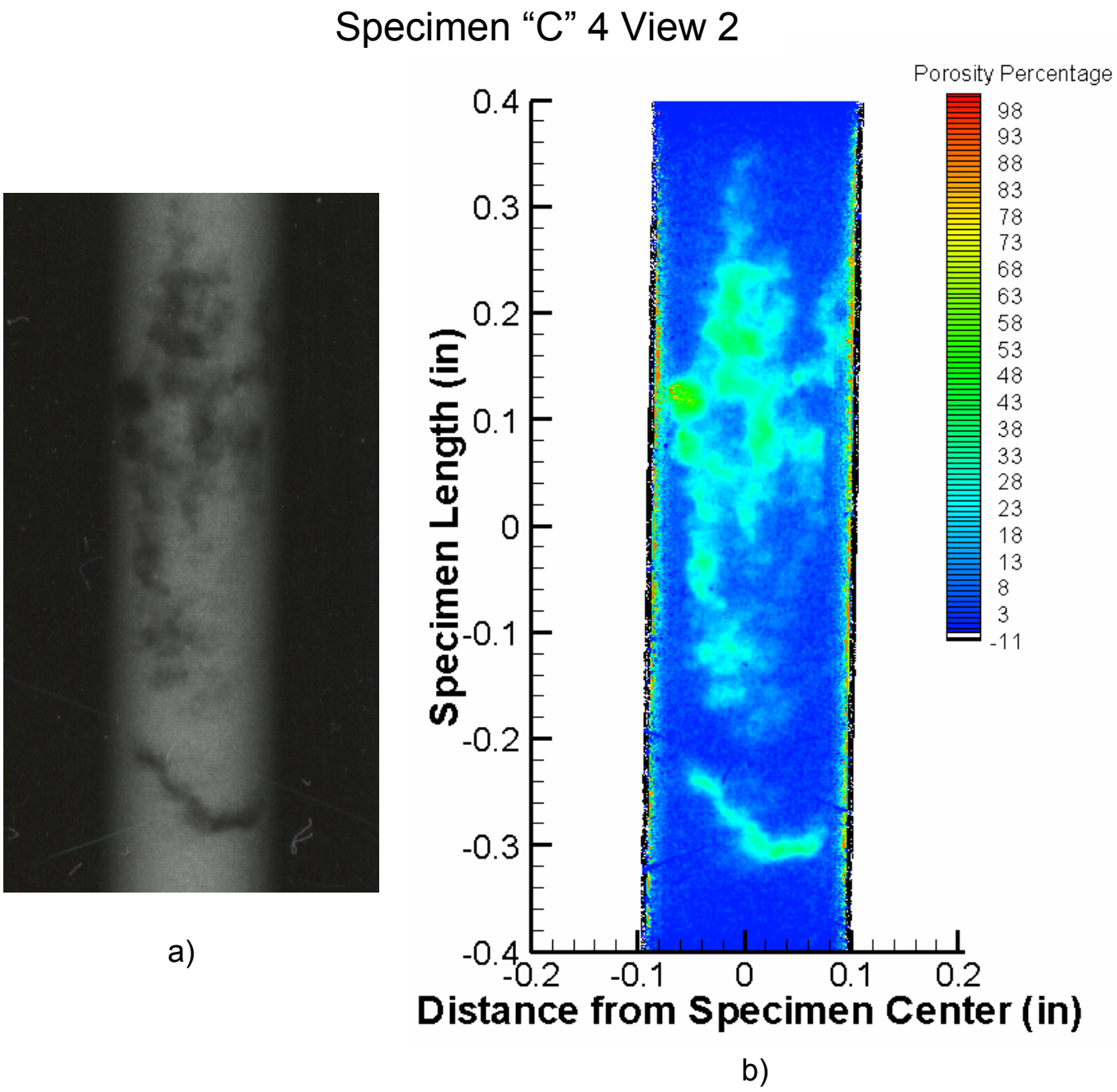


Figure 17 – Comparison between a) radiograph and b) porosity measured from the radiograph for specimen “C” 4, note that areas filtered out from analysis are shown in black in porosity plot

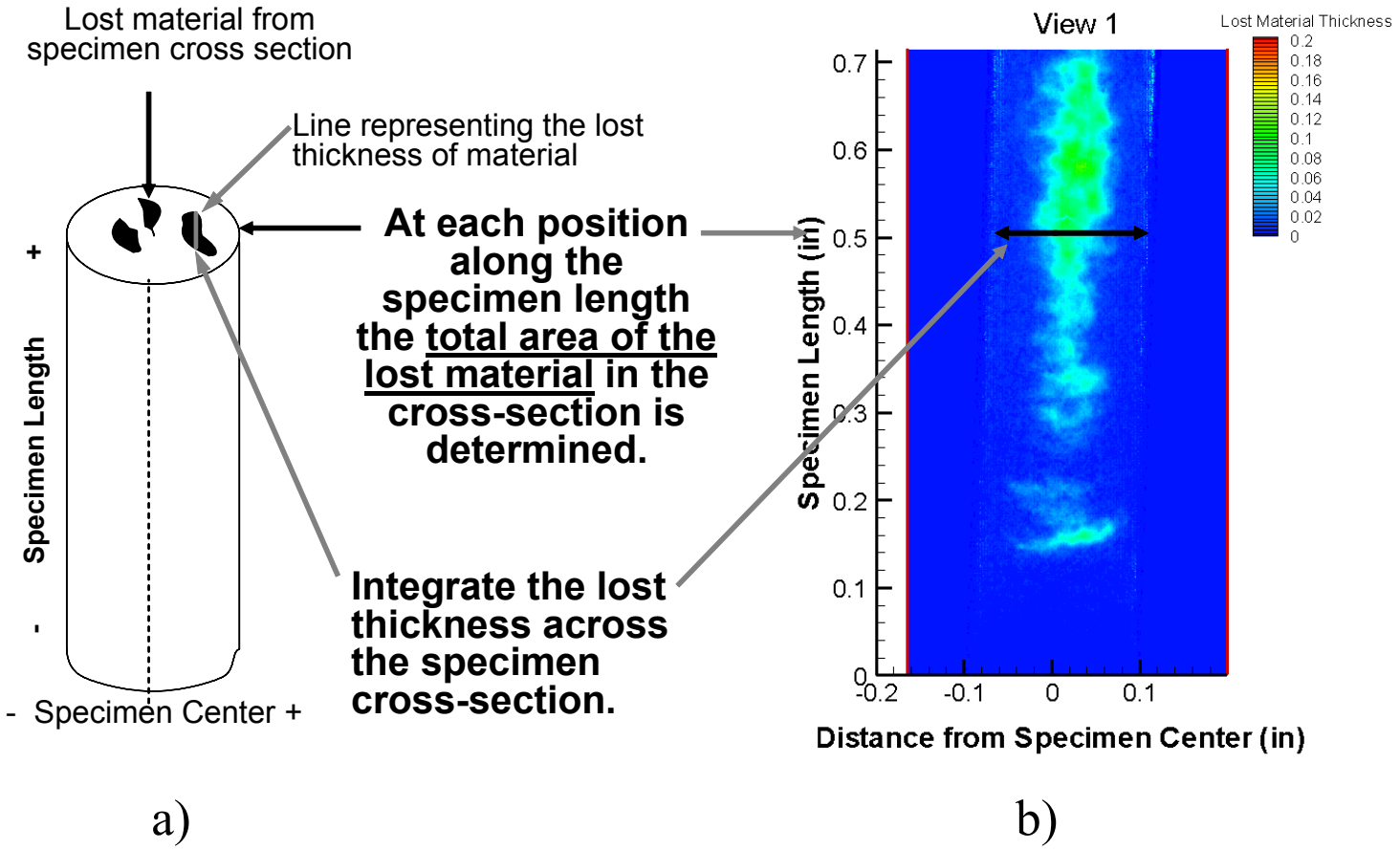


Figure 18 – a) Cross-section at a position along the specimen where lost section thickness $t_{lost}$ is integrated to determine the lost sectional area and area of porosity, and b) a line for specimen "C" 4 along which the $t_{lost}$ is integrated to determine the lost section area due to porosity.

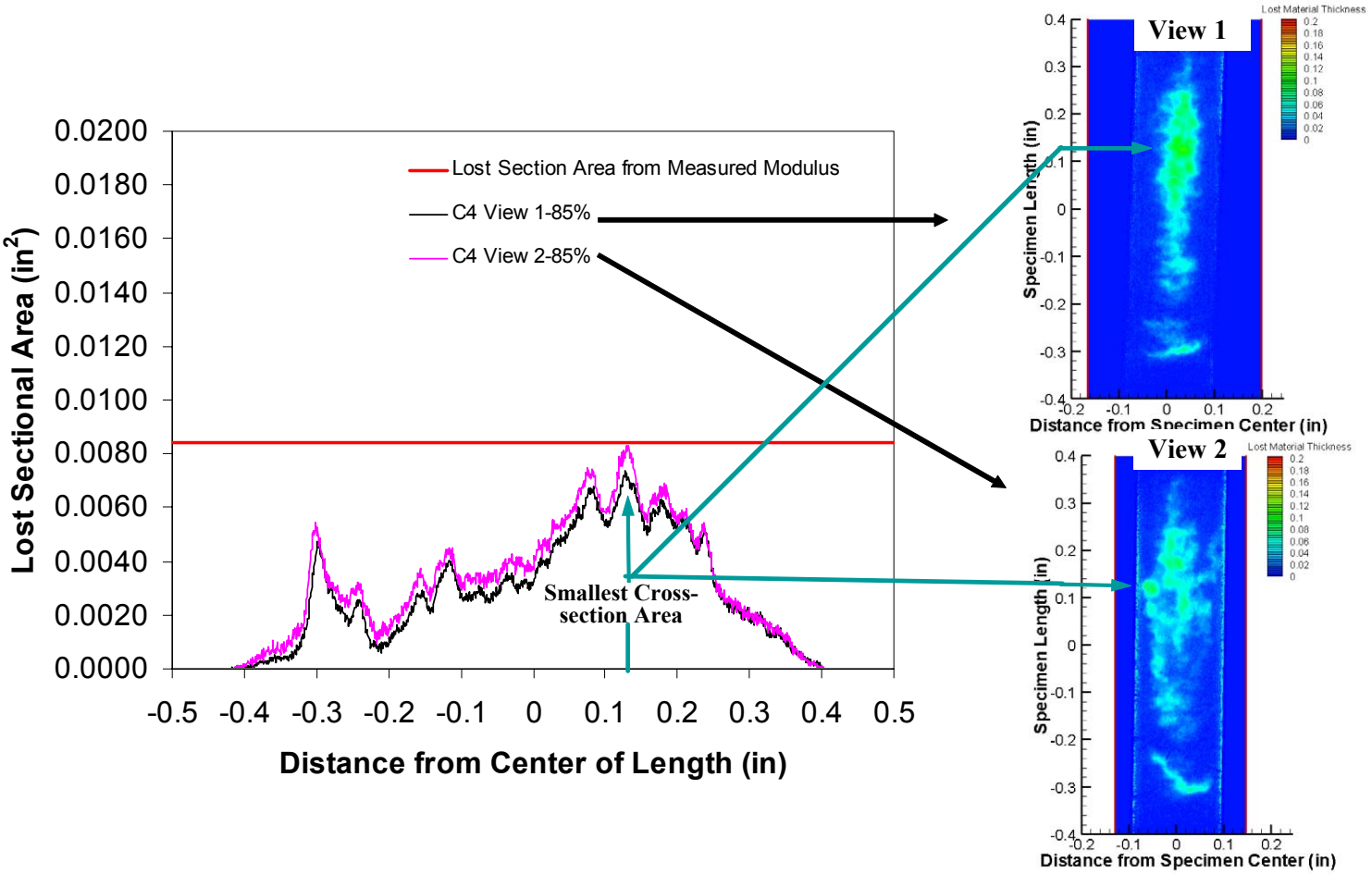


Figure 19 – Lost sectional area of specimen "C" 4 versus position along the specimen length for the two radiographic views shown in Figure 16, the lost section area determined from the measured specimen modulus is also indicated, and the position of the smallest sectional area is indicated in the plots of $t_{lost}$ at the right.

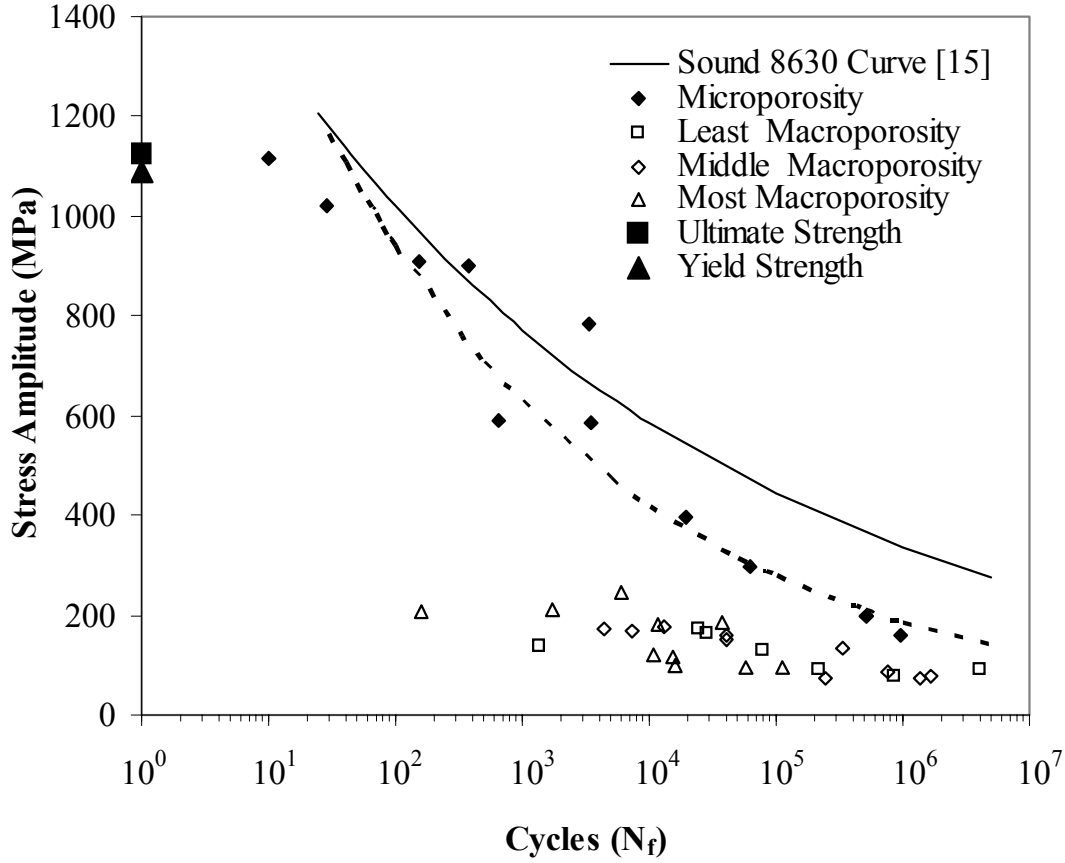


Figure 20 – Stress-Life plot of fatigue test results for 8630 steel test specimens from an earlier study using "sound"/keel block specimens[15], and specimens from the current study with microporosity and macroporosity (separated into least, middle and most specimen types).

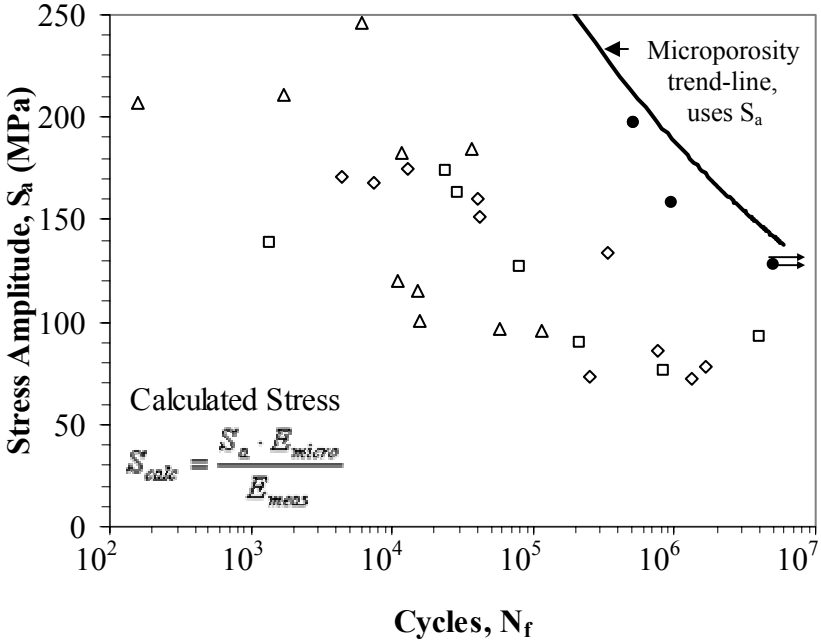


Figure 21 - Stress amplitude for macroporosity data; (□) "least" porosity, (◇) "middle" porosity, (△) "most" porosity; and test stress amplitude data $S_a$ for (●) microporosity material.

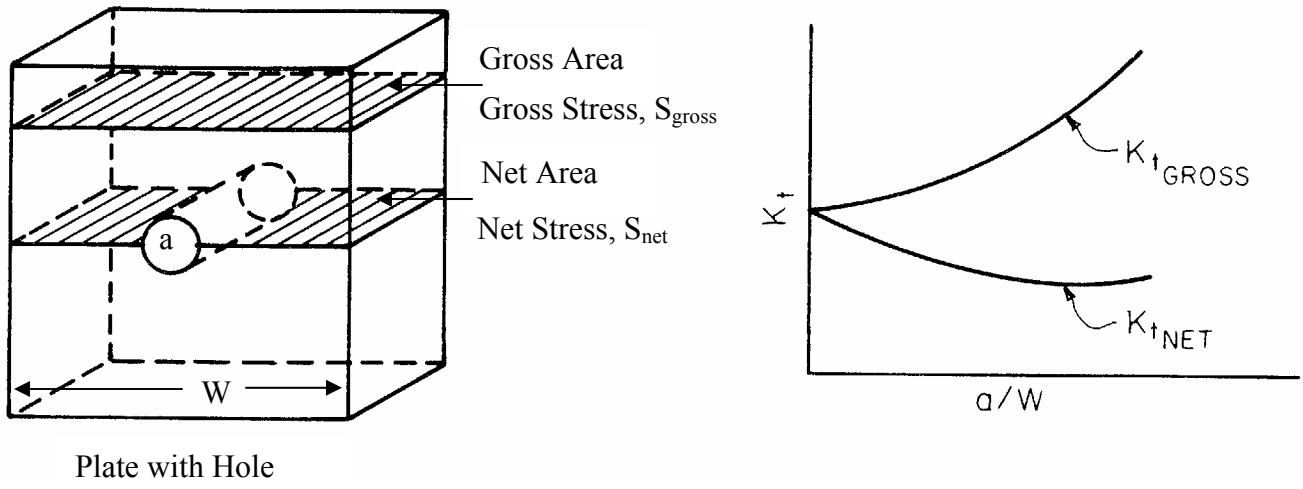


Figure 22 – Definitions of the a) Gross and Net section areas defined for a notch of diameter "a" in a plate of width "W", and b) the behavior of stress concentration factors $K_t$ defined on the basis of Gross and Net section areas versus hole diameter to plate width ratio (Figures from [17]).

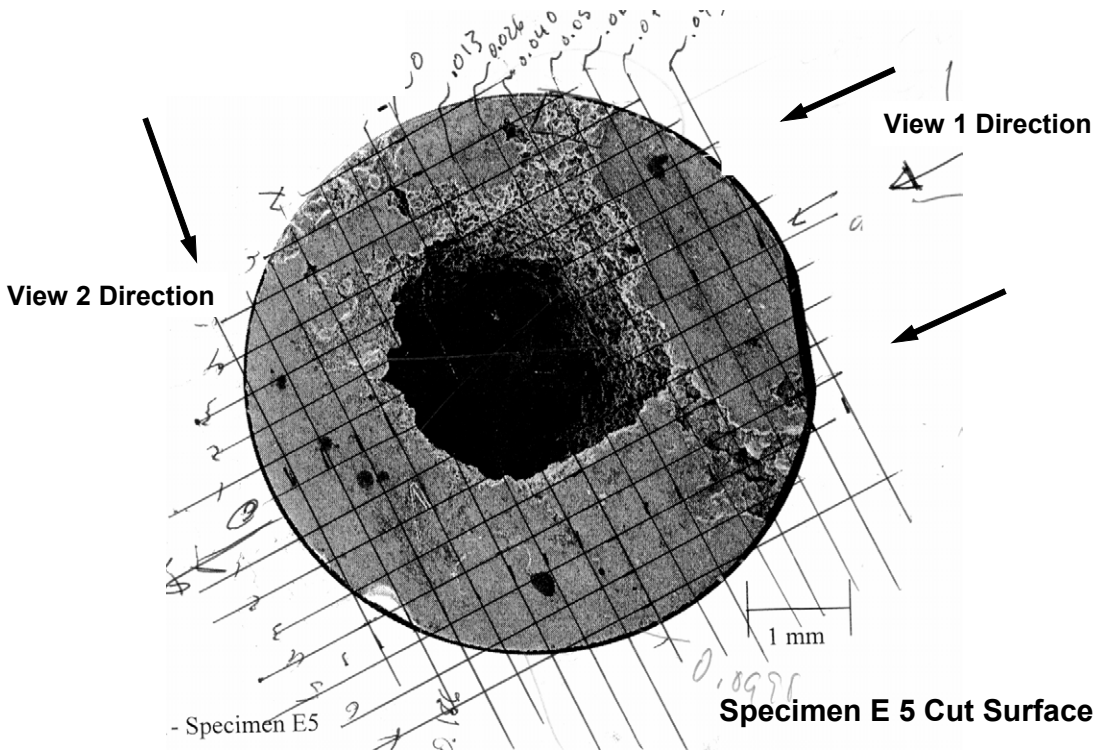


Figure 23 – Image of cut specimen surface with orientations of the two radiographic views shown. Grid is laid out to measure the lost (or void) thickness along the paths of the x-rays through the specimen.

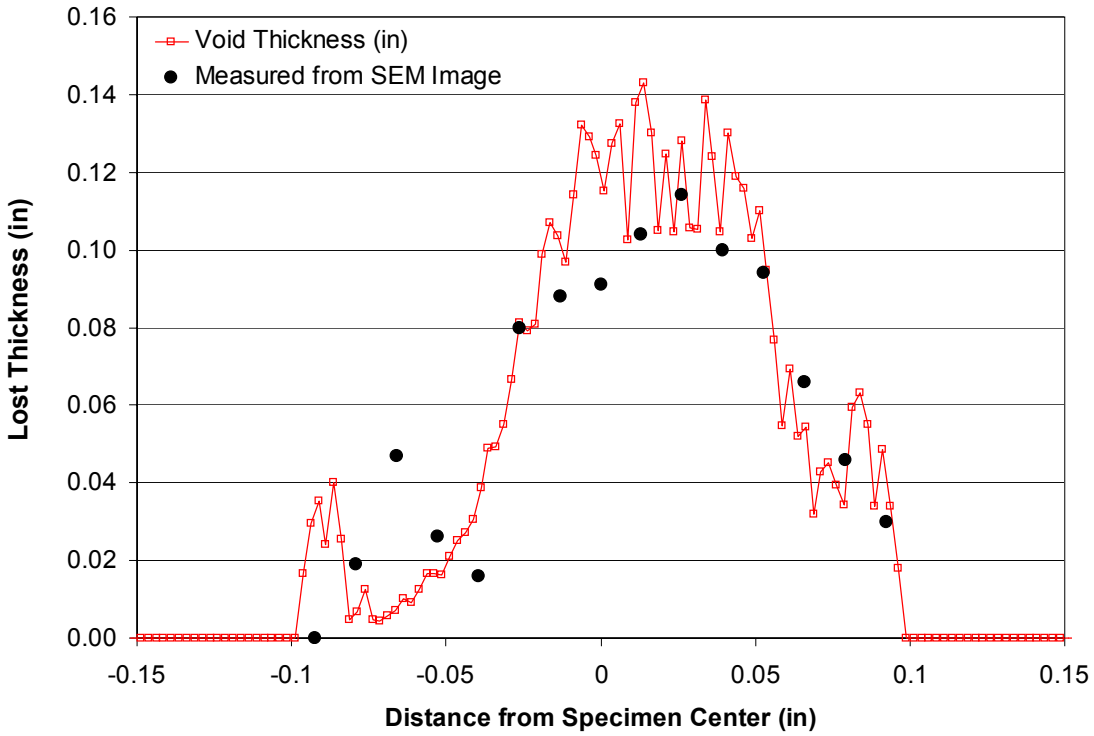


Figure 24 – Comparison for View 1 between the lost (or void) thickness measured from the radiograph at the position of the specimen cut, and from the cut specimen surface shown in Figure 23.

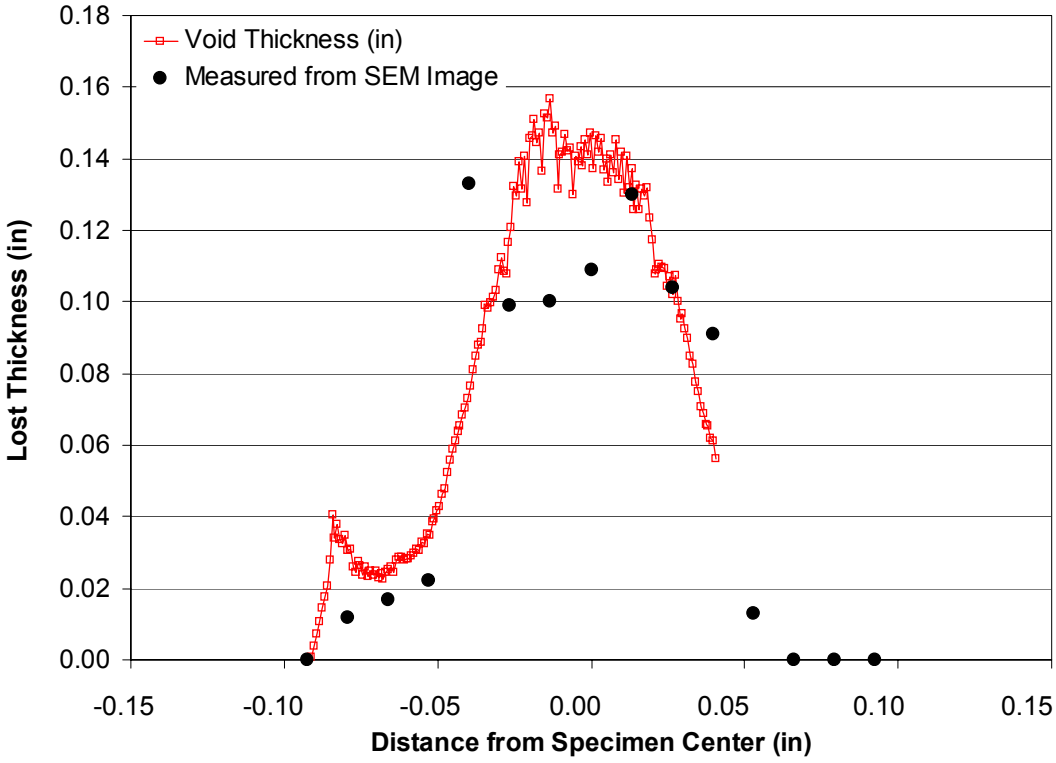


Figure 25 – Comparison for View 2 between the lost (or void) thickness measured from the radiograph at the position of the specimen cut, and from the cut specimen surface shown in Figure 23.

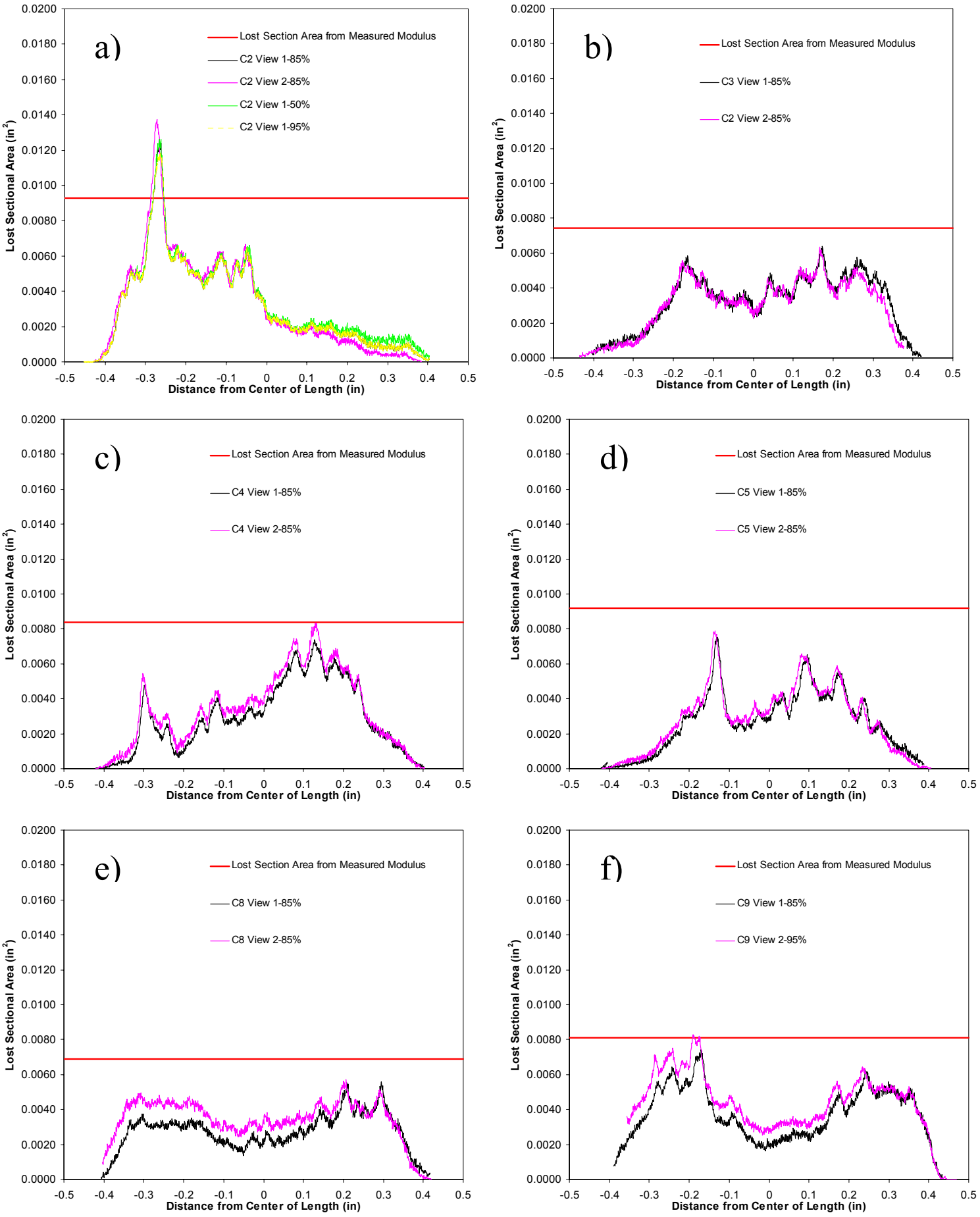


Figure 26 – Lost sectional area distribution along specimen length for two radiographic views, and lost sectional area of specimen calculated from measured specimen modulus for specimens with "least" macroporosity, family "C", a) specimen C2, b) specimen C3, c) specimen C4, d) specimen C5, e) specimen C8, f) specimen C9

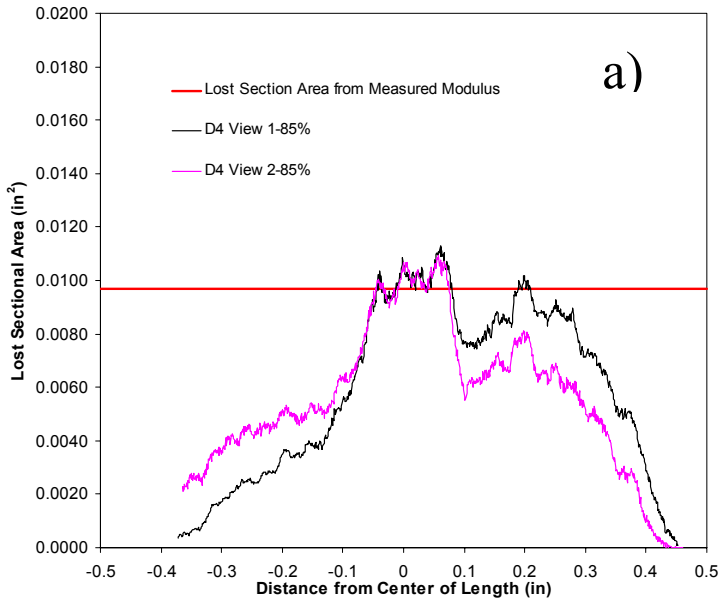


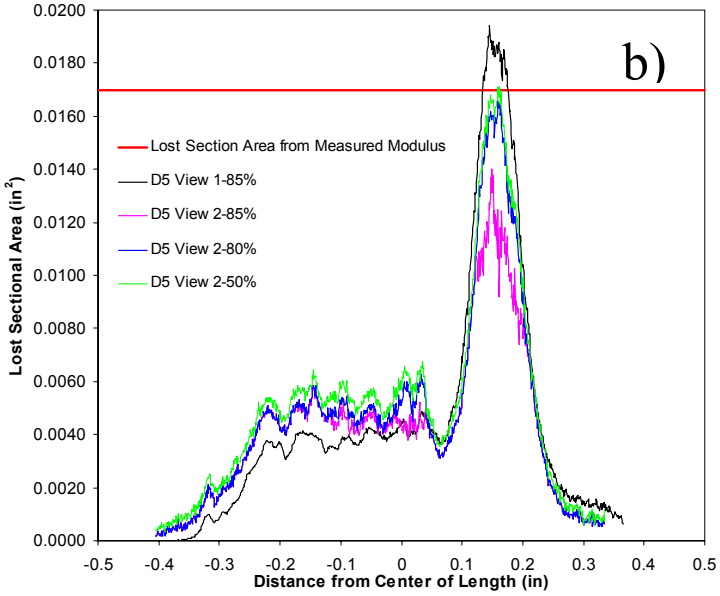


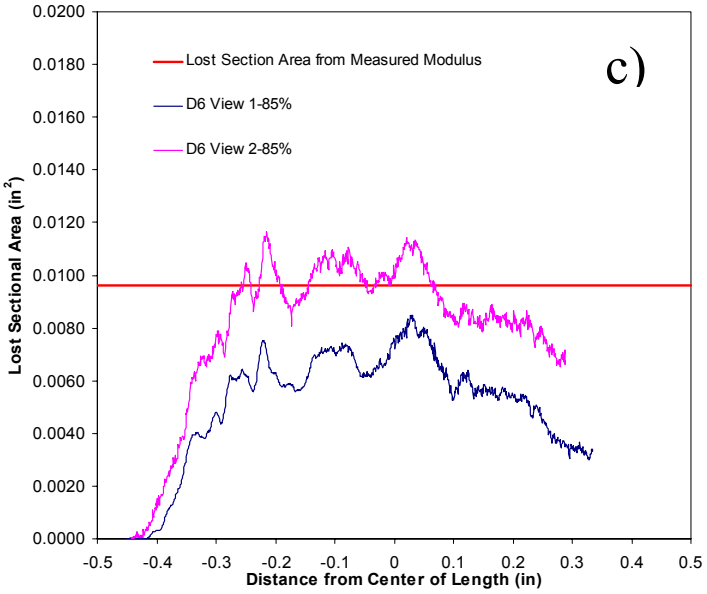


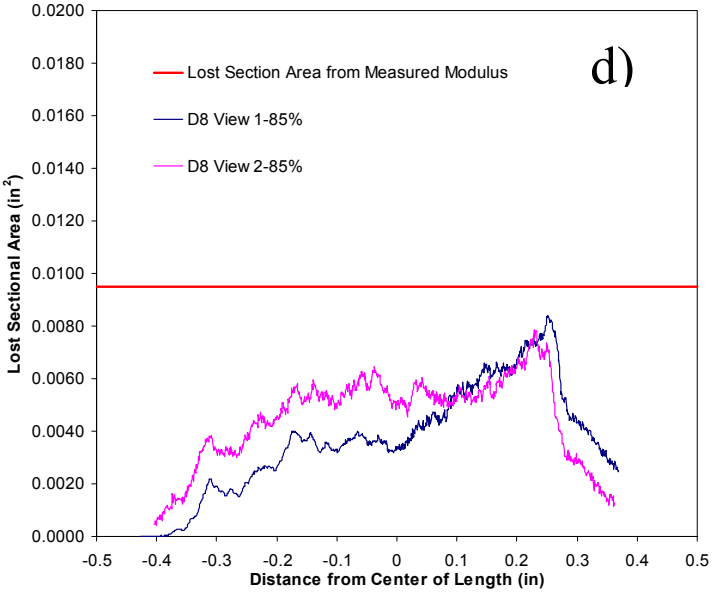


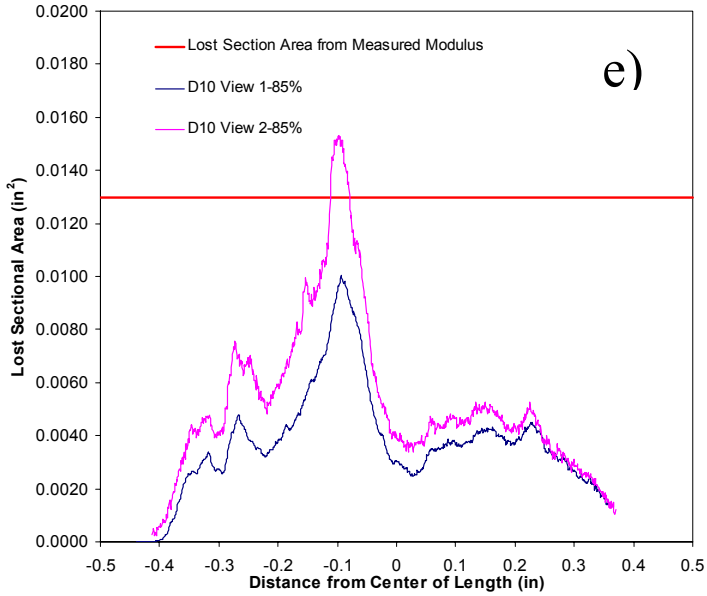


Figure 27 – Lost sectional area distribution along specimen length for two radiographic views, and lost sectional area of specimen calculated from measured specimen modulus for specimens with "most" macroporosity, family "D", a) specimen D4, b) specimen D5, c) specimen D6, d) specimen D8, and e) specimen D10.

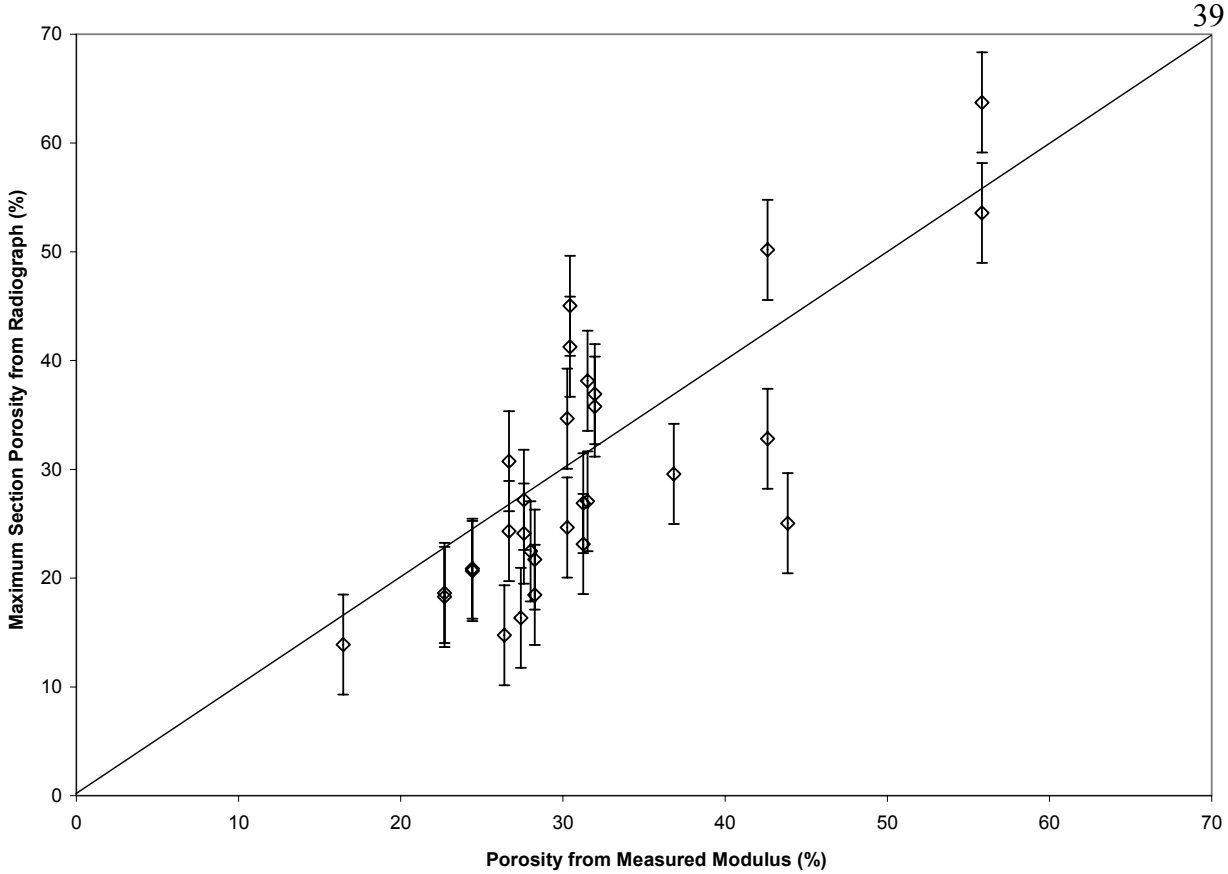


Figure 28 – Maximum cross-sectional porosity occurring in the radiographs versus the specimen porosity determined from the elastic modulus for macroporosity specimens.

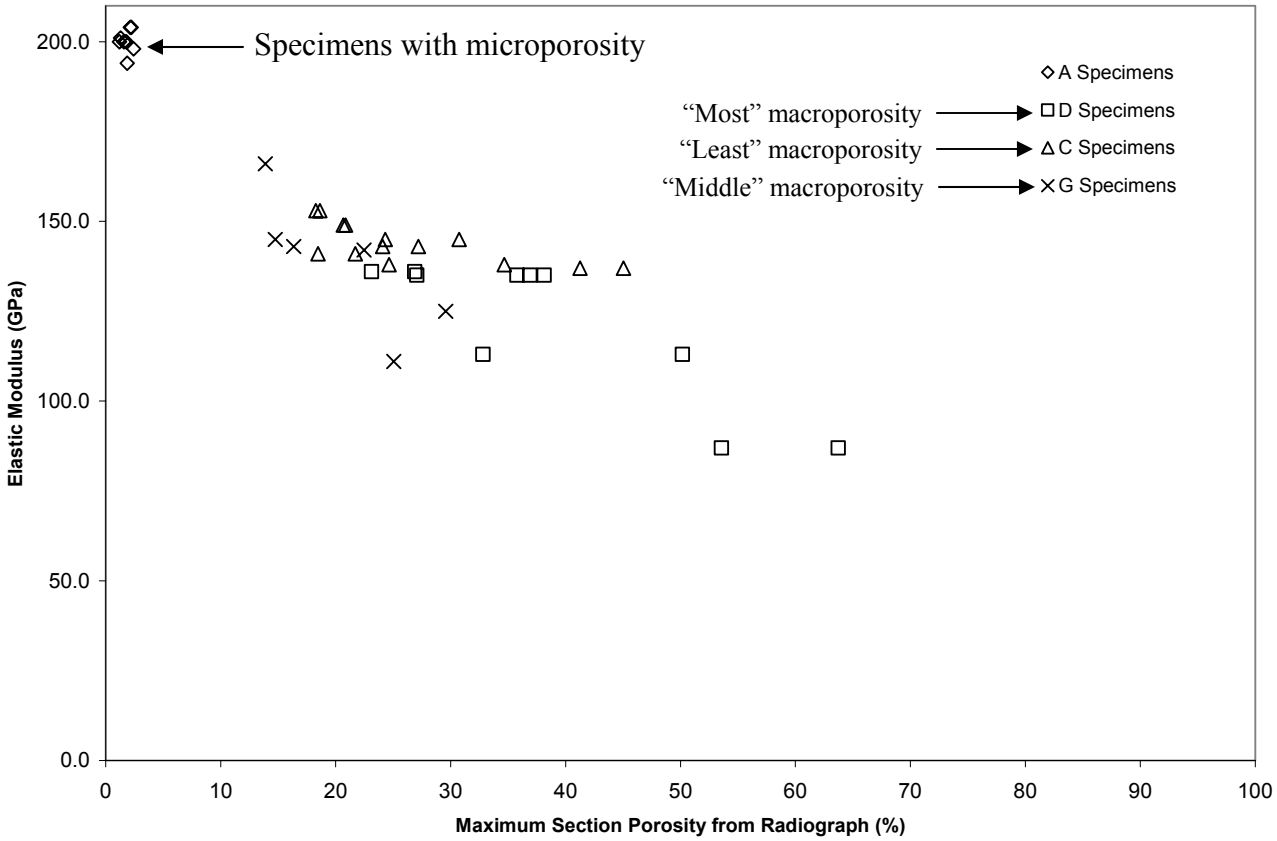


Figure 29 – Measured elastic modulus versus maximum cross-sectional porosity measured from the radiographs.

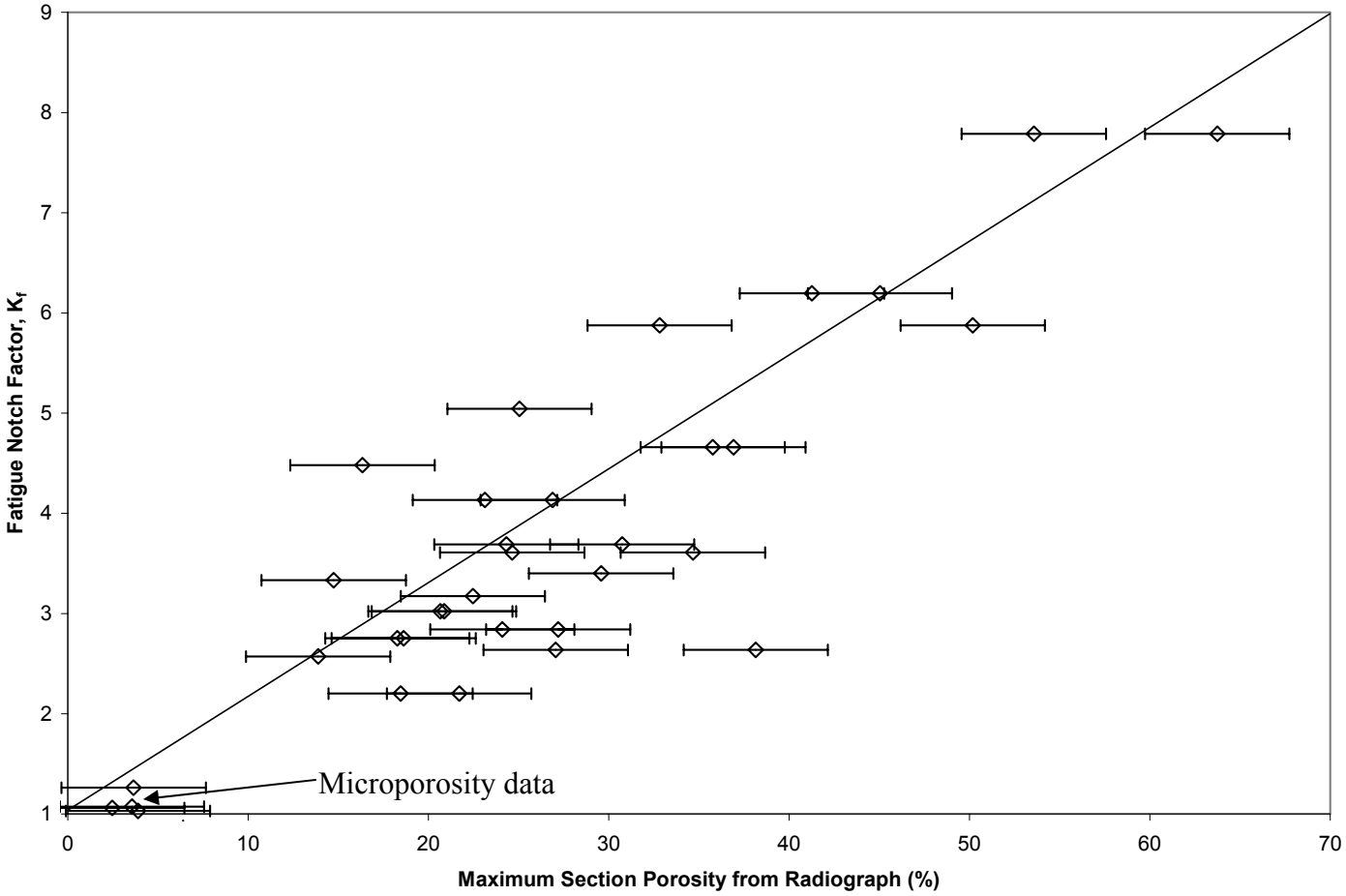


Figure 30 – Fatigue notch factor based on gross section area using the measured specimen modulus versus maximum section porosity determined from the radiographs.

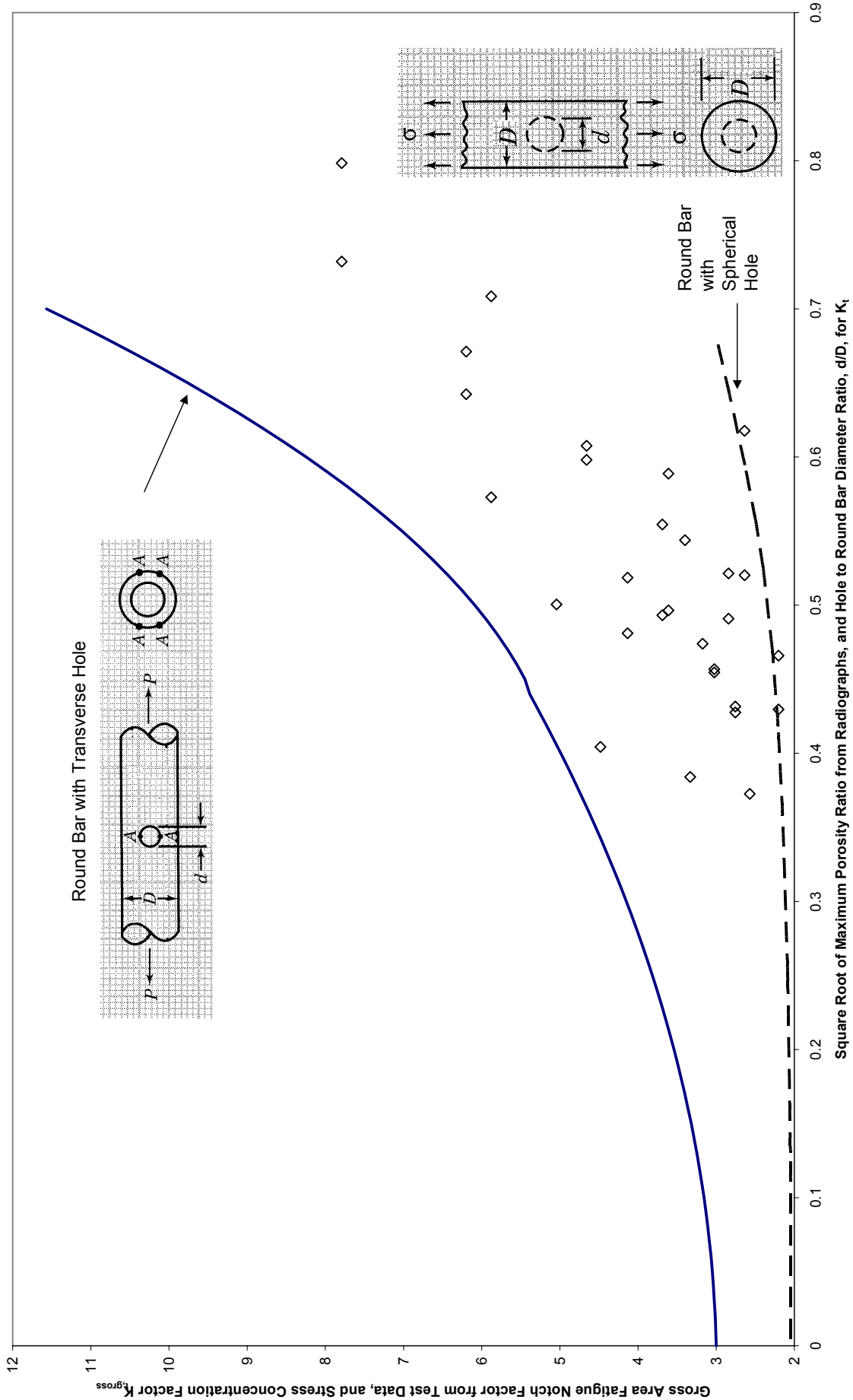


Figure 31 – Data Points: Fatigue notch factor based on gross section area using the measured specimen modulus versus square root of porosity ratio from radiographs. Curves: Stress concentration factors for round bar with transverse hole and spherical hole versus hole diameter to bar diameter ratio.